



Interpreting single-point and two-point focused laser differential interferometry in a turbulent jet

Andrew P. Ceruzzi¹ · Christopher P. Cadou¹

Received: 12 March 2022 / Revised: 25 May 2022 / Accepted: 28 May 2022 / Published online: 1 July 2022
© The Author(s), under exclusive licence to Springer-Verlag GmbH Germany, part of Springer Nature 2022

Abstract

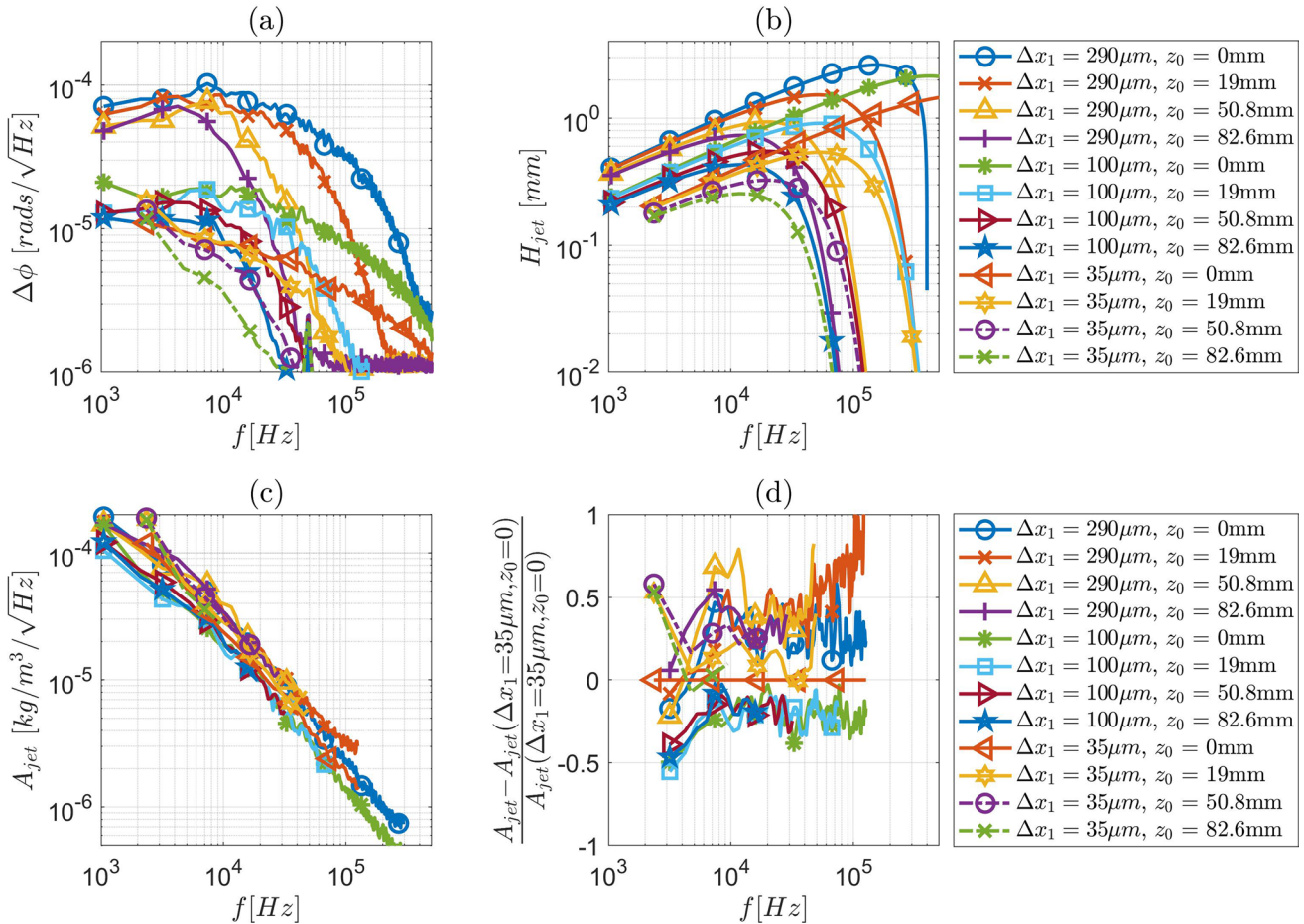
Focused laser differential interferometry (FLDI) and its relative two-point FLDI (2pFLDI) are used to make density fluctuation and velocity measurements, respectively, in a canonical, round turbulent air jet ($U_{\text{jet}} = 300$ m/s, $d = 3.2$ mm, $Re_d = 8.6 \times 10^4$). Both techniques are seedless, non-intrusive, inexpensive (< \$5k), and insensitive to vibrations. The FLDI signal is proportional to the phase difference between two closely spaced laser beams passing through the flow. The phase difference is created by index of refraction gradients in the flow, integrated along the beam paths. Transfer functions for interpreting the FLDI signal are proposed as an accurate method for predicting the response in an arbitrary flow. A procedure for applying these transfer functions to a turbulent jet is developed. The procedure is able to model FLDI's response to fluctuations in the jet with error on the order of 10–50% across a ~ 100 kHz band. The transfer functions provide a simple method for estimating the FLDI & 2pFLDI spatial resolution along the optical axis, which is a strong function of disturbance scale, based on three instrument parameters: (1) the laser wavelength, λ_0 , (2) the beam separation, Δx_1 , and (3) the beam radius at the focus, w_0 . For the 2pFLDI employed in this work ($\lambda_0 = 633$ nm, $\Delta x_1 = 145$ μ m, $w_0 = 3$ μ m), the resolution ranges from 1cm for a 0.9mm disturbance wavelength to 5cm for a 5.5mm disturbance wavelength. The spatiotemporal resolution depends on the convection velocity of the disturbances, as well as the spatiotemporal amplitude variation in the disturbances themselves. We model the velocity and spatial amplitude distribution with Gaussian functions based on historical jet studies and we measure the amplitude variation with frequency directly via FLDI. This leads to 1cm resolution for the smallest timescales measured (100 kHz) up to 5cm resolution for the largest time scales measured (1kHz). 2pFLDI's relatively large spatial resolution complicates comparisons of velocity measurements to those made using hot-wires. The methods, modeling, and procedures outlined in this work provide a framework for interpreting future FLDI and multi-point FLDI measurements.

✉ Andrew P. Ceruzzi
aceruzzi@umd.edu

¹ Department of Aerospace Engineering, University of Maryland, 3179 Martin Hall 4298 Campus Drive, 20740, College Park, MD 20742, USA

Graphical abstract

$$x/d = 20$$



1 Introduction

Forces and heat loads on hypersonic aircraft are strongly influenced by the location of laminar to turbulent transition in the boundary layer (Anderson 2006) and thus are of great interest in the development of hypersonic vehicles. Unfortunately, understanding transition is difficult. Reduced-order models of the boundary layer introduce large uncertainties, and computational costs associated with fully resolving flow around vehicles are prohibitively high. As a result, these locations usually are determined experimentally in wind tunnels (Shea 1988). Understanding transition in hypersonic ground test facilities requires detailed measurements of turbulent inflow conditions (Pate and Schueler 1969; Schneider 2001; Reshotko 2008) but making these measurements is difficult. The disturbances are usually weak ($p'/p_\infty < 1\%$) and occur at frequencies ($\approx 100kHz - 1MHz$) (Boutier

1992) that are beyond the capabilities of traditional intrusive instruments like pitot probes and hot-wires. Intrusive instruments are also generally disadvantageous in these flows because they introduce disturbances unrelated to the problem of interest potentially making it more difficult to interpret experimental results (Bonnet et al. 1998).

Focused Laser Differential Interferometry (FLDI) is a diagnostic tool that has great potential to advance understanding of transition. Its relative, Laser Differential Interferometry (LDI), is a method of measuring density differences in fluid flows first developed by Smeets and George (1971, 1973); Smeets (1977). The LDI signal is proportional to the difference in average density along the optical paths of two closely-spaced laser beams as illustrated in Fig. 1. While very sensitive and capable of operating at frequencies above 10MHz, it is an integrated line of sight measurement and thus offers no spatial resolution along the optical

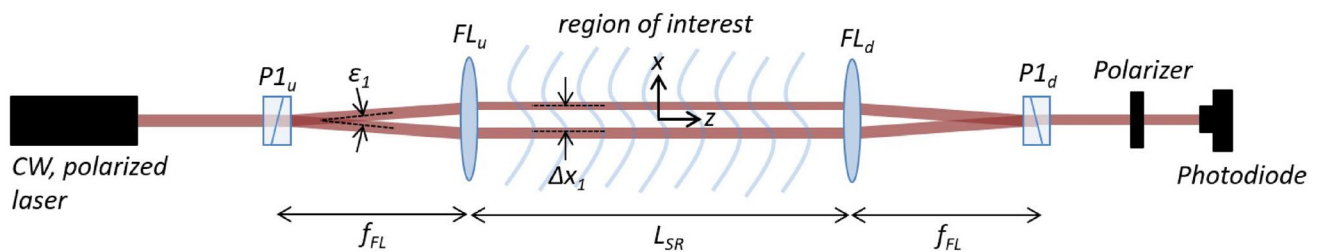


Fig. 1 Schematic illustration of a Laser Differential Interferometer. ($P1_u/P1_d$) upbeam/downbeam birefringent prism with splitting angle (ϵ_1), (FL_u/FL_d) upbeam/downbeam field lens with focal length f_{FL} , (Δx_1) beam separation, (L_{SR}) length of most sensitive region

axis. Smeets sought to correct this deficiency by introducing lenses that brought the two beams to focus in such a way that the beams overlap everywhere except in a small region near the beams' foci. This modification is called FLDI and has the effect of reducing sensitivity to density differences away from the focal region. Smeets also imagined that it would be possible to measure the convection velocity of disturbances by computing the correlation between signals from two FLDI measurement volumes a known distance apart. We call this technique two-point FLDI (2pFLDI).

Advances in laser and data acquisition technology and Parziale's recent success using FLDI to measure free stream disturbances and 2nd-Mode instabilities in a shock tunnel (Parziale 2013; Parziale et al. 2012, 2013, 2014) has renewed interest in FLDI for hypersonic flows. Recent applications of FLDI include work by Benitez et al. (2020), who modified optics to measure 2nd-mode instability amplitudes inside a quiet tunnel with contoured windows, Houpt and Leonov (2021), who employed a cylindrical FLDI in order to probe disturbances near the surface of flat walls, and Birch et al. (2020) who used shrouds to minimize the effect of sidewall turbulence on the FLDI signal. Recent applications of 2pFLDI include those by Jewell et al. (2019), who used a Koester prism to multiplex the FLDI and probe a circular jet, Bathel et al. (2020), who used a Nomarski prism to double the FLDI and measure the disturbance speed of a 2nd mode wave in a Mach 6 flow, and by Ceruzzi et al. (2020), who measured the disturbance velocity profile in a Mach 3 turbulent boundary layer. Also conceived by Smeets and George (1973), multiplexing the FLDI offers an attractive method for simultaneously probing a larger spatial domains and making two-dimensional disturbance velocity measurements. Gragston et al. (2021a, 2021b) demonstrated a method to achieve this using a diffracting optic. Weisberger et al. (2021) demonstrated a multi-point "line FLDI" which uses ovoid beam profiles that are discretely sampled by a photodiode array.

However, and despite all of these applications, there remains no simple, widely accepted method for quantitatively interpreting the FLDI signal and the disturbance velocity measured by 2pFLDI in turbulent flows. In most of

the applications described above, FLDI spectra are presented in arbitrary units or there are large uncertainties in the density fluctuations reported.

Parziale's measurements of free stream fluctuations and 2nd mode waves are an exception but they rely on a separate experiment on a small jet to characterize the FLDI's response function (Parziale 2013). While this approach is reasonable for this particular application, it is not clear that it would work in other flow geometries and it is not clear how the parameters of the jet and of the FLDI affect the calibration. Nevertheless, there have been many excellent efforts to characterize the response of the instrument over the past eight years (Fulghum (2014), Settles and Fulghum (2016), Schmidt and Shepherd (2015), Lawson et al. (2020), Bathel et al. (2021), and Hameed and Parziale (2021)). Fulghum's dissertation (Fulghum 2014) is filled with insights on the FLDI's response including the use of transfer functions to describe how the instrument filters an arbitrary density field. Schmidt and Shepherd also explored similar analytical methods for interpreting the signal (Schmidt and Shepherd 2015) but ultimately concluded that full simulation via ray tracing is the best way to quantitatively interpret the signal. Such simulations are not trivial and thus at present, FLDI remains a qualitative tool that is most useful when compared to itself by offering, for example, a measure of run-to-run variance. Lawson's dissertation, which was recently published, offers a promising example of how analytical methods can be applied to acoustic waves in wind tunnels (Lawson 2021). This work aims to build on Lawson's framework, and apply similar methods to a turbulent jet. The larger goal is to find a general method for interpreting FLDI signals which is easy to use and can be applied in a variety of turbulent flows.

1.1 Objectives

The objectives of this work are to evaluate to what degree transfer functions can be used to model the FLDI's response to a turbulent jet and to investigate the relation between velocities measured using two-point FLDI and velocities measured using other techniques. This will be accomplished by:

1. Building upon the analytical frameworks of others to develop simple, computationally inexpensive, and repeatable methods for interpreting the FLDI signal.
2. Verifying these methods by comparing FLDI measurements of disturbances in a canonical round, subsonic, turbulent air jet to a predicted response using the analytical framework.
3. Comparing 2pFLDI measurements in the canonical jet to historical pitot probe and hot-wire measurements in similar jets.

2 Laser differential interferometry (LDI)

The Laser Differential Interferometry (LDI) signal is proportional to the finite-difference approximation of the density gradient integrated along a line of sight. Figure 1 shows the basic LDI set-up which provides the foundation for FLDI and 2pFLDI. The light source is a monochromatic continuous wave (CW) laser linearly polarized at 45° with respect to the axis that defines the gradient of interest. A birefringent prism ($P1_u$) splits the beam into two equally intense orthogonally polarized beams with a small inter-beam angle (ϵ_1). A field lens (FL_u) located one focal length (f_{FL}) downstream of the prism arrests the inter-beam divergence and fixes the distance between the two beams (Δx_1). This distance is given by:

$$\Delta x_1 = 2f_{FL} \tan\left(\frac{\epsilon_1}{2}\right). \tag{1}$$

The beams propagate through a region of interest of length (L_{SR}) where index of refraction gradients ($\frac{\partial n}{\partial x}$) create an optical path difference - and thus a phase shift ($\Delta\phi$) - between the beams. The relationship between density and index of refraction is given by the Gladstone-Dale relation:

$$n = 1 + \beta \frac{\rho}{\rho_s}, \tag{2}$$

where (β), the Gladstone-Dale constant, is a function of gas composition and light wavelength (p. 154, Liepmann and Roshko 1957) and (ρ_s) is density at 0°C and 760mmHg ($1.2923\text{kg}/\text{m}^3$ for air). The orthogonally polarized beams are recombined by a field lens (FL_d) and birefringent prism ($P1_d$) identical to FL_u and $P1_u$ but operating in reverse. The recombined beams pass through a polarizer aligned with the laser polarization (45° from the splitting axis) allowing the beams to interfere. The intensity of light (I_{PD}) incident on the photodiode is a function of the phase shift as follows:

$$I_{PD} = 2I_b(1 + \cos(\Delta\phi)), \tag{3}$$

where (I_b) is the intensity of a single beam (e.g., Born and Wolf 1980, p. 259). In practice, perfect interference contrast

is not achievable and the intensity will not reach zero when $\Delta\phi = \pi$. Also, high-frequency signals will be attenuated by the photodiode circuit’s response. Thus, the voltage output from the photodiode (V) is expressed as:

$$V = \frac{1}{2} [V_{max} + V_{min} + (V_{max} - V_{min}) \cos(\Delta\phi)H_{PD}], \tag{4}$$

where H_{PD} is a transfer function that accounts for the photodiode circuit’s response.

Voltage is plotted as a function of phase difference in Fig. 2. Using the same terminology as Parziale et al. (2012), we define

$$V_0 = \frac{V_{max} + V_{min}}{2}. \tag{5}$$

Adjusting the phase by translating $P1_u$ or $P1_d$ along the x-axis so that $V = V_0$ ensures that the instrument’s response is approximately linear over its sensitive region i.e. $V - V(t = 0) \approx c[\Delta\phi - \Delta\phi(t = 0)]$ where c is a constant. This adjustment is critical because it maximizes sensitivity, simplifies interpretation of the signal, and minimizes the likelihood of phase ambiguity which occurs when the signal reaches V_{max} or V_{min} during an experiment. The relationship between voltage measured over time and phase difference can now be written as

$$V(t) = V_0 + V_0 \sin(\Delta\phi(t))H_{PD}. \tag{6}$$

Fulghum measured the response of the same detector system used in this work (a ThorLabs DET36 photodiode with a 1kΩ resistor) to a LED pulsed square wave for frequencies to 500kHz (Fulghum 2014) and found it to be flat. Thus, we assume

$$H_{PD} = 1 \text{ for } f < 500\text{kHz} \tag{7}$$

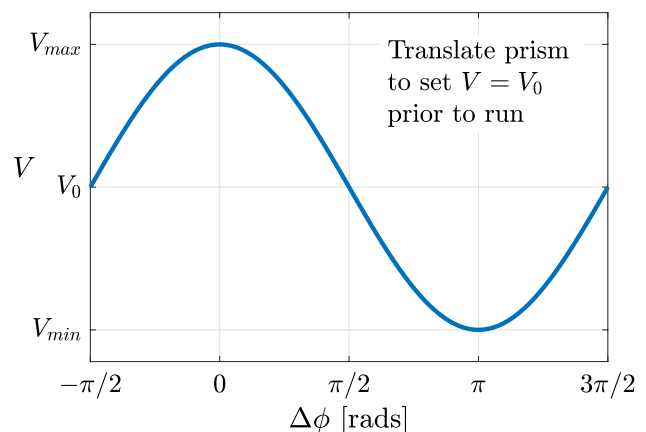


Fig. 2 Relationship between measured voltage (V) and phase difference between beams ($\Delta\phi$)

which means that we can ignore the response of the photodiode circuit. This allows us to write

$$\Delta\phi(t) = \arcsin\left(\frac{V(t)}{V_0} - 1\right), \tag{8}$$

which is a common assumption in other FLDI work (Parziale et al. 2014; Schmidt and Shepherd 2015; Benitez et al. 2020; Birch et al. 2020).

For two beams traversing paths s_1 and s_2 respectively, the phase difference at the detector face ($s = D$) associated with the index of refraction field $n(\mathbf{x})$ is given by

$$\Delta\phi(t) = \frac{2\pi}{\lambda_0} \int \int_D I_0 \left[\int_{s_1}^D n(\mathbf{x}_1, t) ds_1 - \int_{s_2}^D n(\mathbf{x}_2, t) ds_2 \right] d\xi d\eta, \tag{9}$$

where (λ_0) is the laser wavelength, S is the location of the light source, $\mathbf{x}_i(s_i) = (x_i, y_i, z_i)$, and $I_0(\xi, \eta)$ is the intensity on the detector face when there is no phase difference between the two beams. ξ and η are coordinates which map the detector surface. Equation 9 describes a general interferometer and is taken directly from Schmidt and Shepherd (2015) who derived it from Born and Wolf (1980). One can solve for the exact phase change provided a complete, well-resolved solution for $n(\mathbf{x})$ is available. However, there is no way to solve Eq. 9 in the other direction i.e. for $n(\mathbf{x})$ from $\Delta\phi(t)$. This is because many refractive fields can result in the same measured phase difference. Thus, in order to invert Eq. 9 and solve for some aspect of the refractive field, we must make assumptions about the field itself.

Previous work (Schmidt and Shepherd 2015) has modeled disturbances as sinusoidal waves with frequency-dependent amplitudes that vary in time and in space but only along the flow direction (x). Lawson (2021) extends this analysis to account for waves propagating at any angle. While this may be appropriate for homogeneous free-stream turbulence and acoustic noise, it may be less so for flows with substantial variations along the beam direction (z). Fulghum (2014) suggested modeling an amplitude variation with z , such as a Gaussian model for a jet, but he did not suggest accounting for a variation in the local convective velocity with z , i.e. $u_c(z)$. Building on these previous works, we propose the following model for the density field

$$\rho(x, y, z, t) = g(z) \int_{-\infty}^{\infty} A(f) e^{i(k_x x - 2\pi ft + \psi)} df \tag{10}$$

where k_x is the disturbance wavenumber oriented parallel to the flow direction (x), $\psi = \psi(f)$ is the disturbance phase, $A(f)$ is the disturbance amplitude (which depends on the frequency f), and $g(z)$ is a unit-less function which models the disturbance amplitude variation with z , averaged across all frequencies. Wavenumber is defined as

$$k_x = 2\pi f / u_c. \tag{11}$$

where u_c is the streamwise convection velocity of a disturbance. The simultaneous use of $g(z)$ and allowing the disturbance convective velocity to vary with z , i.e. $u_c = u_c(z)$ differentiates this model from those used in previous work. Its efficacy will be verified later via comparison to measurements in a turbulent jet.

The intensity distribution in the beam is modeled as

$$I_0(r, \theta) = \frac{2}{\pi w^2} \exp\left(-\frac{2r^2}{w^2}\right), \tag{12}$$

where w is the Gaussian beam radius parameter (Siegman 1986). The polar coordinates r and θ are related to the Cartesian coordinates

$$x = r \cos \theta \tag{13}$$

$$y = r \sin \theta. \tag{14}$$

If we restrict ourselves to the region between field lenses FL_u and FL_d , the paths of complimentary rays in the interferometer can be parameterized by the z -axis and written as

$$\mathbf{x}_1(z) = \left(x + \frac{\Delta x_1}{2}, y, z\right) \tag{15}$$

$$\mathbf{x}_2(z) = \left(x - \frac{\Delta x_1}{2}, y, z\right). \tag{16}$$

Inserting the Gladstone-Dale relation (Eq. 2) into Eq. 9, rewriting the 2-D integral in polar coordinates, and exchanging the order of integration yields the following expression for the phase difference measured by the instrument in terms of the local density field:

$$\Delta\phi(t) = \frac{2\pi\beta}{\lambda_0\rho_s} \int_{-L_{SR}/2}^{L_{SR}/2} \left[\int_0^{2\pi} \int_0^\infty I_0\rho(\mathbf{x}_1, t) r dr d\theta - \int_0^{2\pi} \int_0^\infty I_0\rho(\mathbf{x}_2, t) r dr d\theta \right] dz. \tag{17}$$

Introducing the model of the density field (Eq. 10), Equation 11-16, and simplifying the integrand analytically leads to:

$$\Delta\phi(t) = \frac{2\pi\beta}{\lambda_0\rho_s} \int_{-L_{SR}/2}^{L_{SR}/2} \left[g(z) \int_{-\infty}^{\infty} 2A(f) \times \sin\left(\frac{k_x \Delta x_1}{2}\right) \exp\left(-\frac{k_x^2 w^2}{8}\right) e^{-2\pi ift} i e^{i\psi} df \right] dz. \tag{18}$$

where $A(f)$ is the spectral density of the disturbance amplitude averaged over the beam path z . The details are presented

in Appendix A. This form is useful because it isolates the effects of the beam spacing (Δx_1) and the beam radius (w) on the signal through the sinusoidal and exponential functions in the integrand. It is convenient to represent these dependencies as transfer functions $H_{\Delta x}$ and H_w respectively where

$$H_{\Delta x} = \sin\left(\frac{k_x \Delta x_1}{2}\right) = \sin\left(\frac{\pi f \Delta x_1}{u_c}\right), \tag{19}$$

and

$$H_w = \exp\left(-\frac{k_x^2 w^2}{8}\right) = \exp\left(-\frac{\pi^2 w^2 f^2}{2u_c^2}\right) \tag{20}$$

These functions have been derived in previous works (Parziale et al. 2014; Fulghum 2014; Schmidt and Shepherd 2015; Lawson et al. 2020) using slightly different definitions and terminologies. For example, $H_{\Delta x}$ is equivalent to the correction factor c in Parziale et al. (2012) and $(H_s \frac{i\omega \Delta x}{2c_r})$ in Schmidt and Shepherd (2015). Schmidt refers to this as the differentiation performed by the instrument. H_w describes the spatial filtering caused by integrating over the local beam intensity profile $I_0(r, \theta)$. Fulghum (2014) and Schmidt and Shepherd (2015) derive the version of Eq. 20 based on the disturbance wavenumber (k_x) and beam radius parameter (w). The version of Eq. 20 that uses the disturbance frequency (f) and its convective velocity (u_c) is not presented in these works, though it is implied. All approaches assume that the disturbances are sinusoidal. A concise validation of Eq. 20 was recently performed by Lawson et al. (2020) using acoustic waves.

Returning to Eq. 18, we exchange the order of integration again and use the transfer functions as short-hand to write:

$$\Delta\phi(t) = \frac{4\pi\beta}{\lambda_0\rho_s} \int_{-\infty}^{\infty} A(f) \int_{-L_{SR}/2}^{L_{SR}/2} (g(z)H_{\Delta x}H_w) dz \times e^{-2\pi ift} i e^{i\psi} df \tag{21}$$

Note the similarity of Eq. 21 to the Fourier transform of a time dependent signal:

$$\mathcal{F}[] = \int_{-\infty}^{\infty} [] e^{2\pi ift} dt. \tag{22}$$

Taking the Fourier transform of Eq. 21 eliminates the $e^{-2\pi ift}$ term. If we restrict our interest to the magnitude of disturbances (i.e the magnitude of the Fourier transform) and make the additional assumption that phases of the disturbances $\psi(f)$ are random and uncorrelated which is a reasonable assumption in many turbulent flows (see Chapter 5 of (Lawson 2021)), then $|ie^{i\psi}| = 1$ and Eq. 21 becomes:

$$\mathcal{F}[\Delta\phi] = \frac{4\pi\beta}{\lambda_0\rho_s} A(f) \int_{-L_{SR}/2}^{L_{SR}/2} |g(z)H_{\Delta x}H_w| dz. \tag{23}$$

Eq. 23 is a concise description of the response of the LDI instrument to a flow whose density field can be modeled by Eq. 10. The left-hand-side is the Fourier transform of the measured signal. The right hand side is the response of the instrument which is a function of three instrument parameters:

1. λ_0 —the laser wavelength
2. Δx_1 —the beam separation
3. w —the local beam radius

and three flow field parameters:

1. $g(z)$ —frequency-averaged density disturbance amplitude variation with z .
2. $u_c(z)$ —convective (x -axis) disturbance velocity variation with z .
3. $A(f)$ —density disturbance amplitude spectral density.

All instrument parameters are constant across the interval $-L_{SR}/2 \leq z \leq L_{SR}/2$ in the LDI system illustrated in Fig. 1. Thus, any variation in sensitivity along the optical axis is caused by flow parameters only. This poses a problem in wind tunnel applications where strong fluctuations associated with turbulence along the tunnel walls can overwhelm the signals from the weaker fluctuations in the core flow that are of interest. This is a problem that affects all line of sight optical techniques.

2.1 Focused laser differential interferometry (FLDI)

FLDI is a variant of LDI designed to overcome the line of sight problem. It works by expanding the interferometer beams to large diameters and then focusing them such that they overlap along most of their optical paths save for small regions near the focal points. This has the effect of limiting the sensitive region (L_{SR}) to a small area around the focal points. A schematic illustration of the FLDI instrument is presented in Fig. 3. An objective lens (OL) with short focal length (f_{OL}) located at a distance $f_{OL} + L_o$ up-beam of the field lens expands the beams so that they overlap substantially reaching a max diameter (D_{FL}) at the field lens. The field lens focuses the beams at a distance L_i down-beam of the field lens. The relationship between L_o , L_i , and f_{FL} is given by the thin lens equation,

$$\frac{1}{L_o} + \frac{1}{L_i} = \frac{1}{f_{FL}}. \tag{24}$$

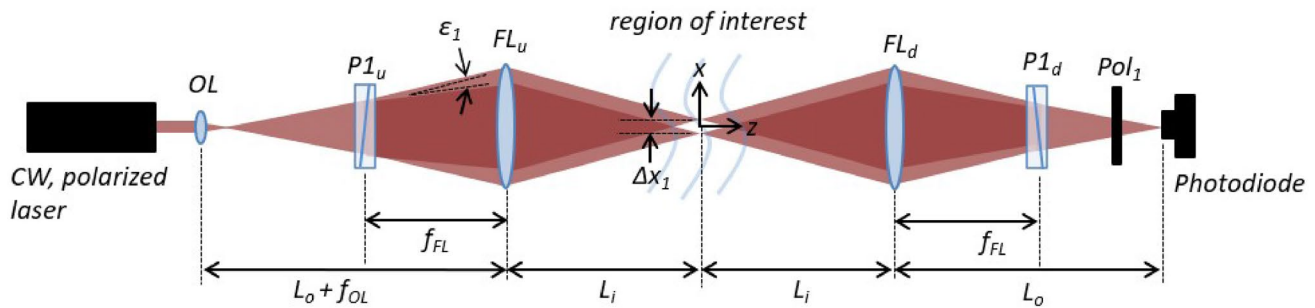


Fig. 3 Schematic illustration of a Focused Laser Differential Interferometer. (OL) objective lens, (P1_u/P1_d) upbeam/downbeam birefringent prism with splitting angle (ε₁), (FL_u/FL_d) upbeam/downbeam

field lens with focal length f_{FL} , (Pol₁) polarizer rotated 45° from x-axis, (L_o) distance from objective lens focus to field lens, (L_i) distance from field lens to focus, (Δx₁) beam separation

A comprehensive guide to design, alignment, and calibration of FLDI is provided by Neet et al. (2021).

The only difference between LDI and FLDI is that the beam diameter is now a function of distance along the optical axis, i.e. $w = w(z)$. This function is given by

$$w(z)^2 = w_0^2 \left[1 + \left(\frac{\lambda_0 z}{\pi w_0^2} \right)^2 \right], \tag{25}$$

where w_0 is the beam radius at the focus ($z = 0$) (Siegman 1986). w_0 can be determined by measuring the beam diameter at any known position z and solving Eq. 25 for w_0 . Several measurements are better than one for determining w_0 . Substituting Eq. 25 into Eq. 20 gives:

$$H_w = \exp \left\{ -\frac{k_x^2 w_0^2}{8} \left[1 + \left(\frac{\lambda_0 z}{\pi w_0^2} \right)^2 \right] \right\} \tag{26}$$

With this context, let us re-examine Eq. 23 applied to the region between the field lenses of an FLDI:

$$\mathcal{F}[\Delta\phi] = \frac{4\pi\beta}{\lambda_0\rho_s} A(f) \int_{-L_i}^{L_i} |g(z)H_{\Delta x}H_w| dz. \tag{27}$$

The right hand side describes the attenuation of the true density fluctuation spectrum by the instrument. $H_{\Delta x}$ captures the effect of beam separation which attenuates response as the disturbance wavenumber moves away from $\pi/\Delta x_1$. H_w captures the effect of focusing which causes high wavenumbers to be attenuated faster than smaller ones as one moves away from the focus. The combined effects of $H_{\Delta x}$ and H_w on the response of the FLDI used in this work are illustrated in Fig. 4 which is a contour plot of the response of the instrument as a function of distance along the optical axis (z -direction) and the wavenumber of the disturbance. The depth of focus in the z -direction (taken as the full-width half max of

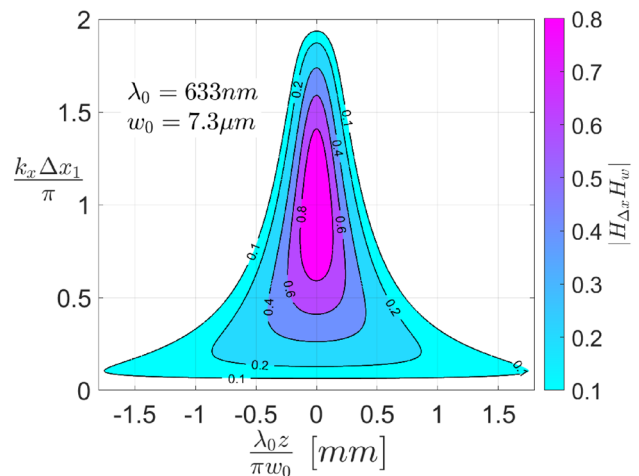


Fig. 4 Variation of the product of FLDI transfer functions $H_{\Delta x}H_w$ with wavenumber and z for $\lambda_0 = 633\text{nm}$, $w_0 = 7.3\mu\text{m}$

$H_{\Delta x}H_w$) is $\sim \frac{\pi w_0}{2\lambda_0} \text{mm}$ for $k_x = \pi/\Delta x_1$ and improves slightly as wavenumber increases (wavelength decreases). As wavenumber decreases below $\pi/\Delta x_1$ resolution degrades while the overall response decreases. This has the effect of reducing the range of wavenumbers to which the instrument is sensitive far from the focus.

In order to assess FLDI’s temporal resolution, some modeling or measurement of u_c is required in order to convert wavenumbers to frequencies. Using Eq. 11 for this purpose leads to a new expression for the beam radius transfer function:

$$H_w = \exp \left(-\frac{\pi^2 w_0^2 f^2}{2u_c^2} - \frac{\lambda_0^2 f^2 z^2}{2w_0^2 u_c^2} \right). \tag{28}$$

One objective of this work is to understand if the combined transfer function, $H_{\Delta x}H_w$ accurately models the FLDI’s

response to a turbulent air jet. To do this, we define the “FLDI-jet sensitivity function”:

$$H_{jet} = \int_{-L_i}^{L_i} |g_{jet}(z)H_{\Delta x}H_w| dz. \tag{29}$$

To evaluate this integral, we need estimates of $g_{jet}(z)$ and $u_c(z)$ for the flow field. These are readily available in the literature for turbulent jets which is why we will use a turbulent jet to validate our theory. The schematic illustration of the FLDI probe beam relative to the round turbulent jet presented in Fig. 5 is useful for understanding the relationship between the FLDI and the parameters describing the turbulent jet. The Reynolds number of the jet we will use to validate the instrument function is 8.55×10^4 . Measurements by Hinze in a round turbulent jet at similar Reynolds number ($Re_d = 6.7 \times 10^4$, Hinze and Van Der Hegge Zijnen (1949)) show that the radial density profiles at different downstream distances x follow Gaussian distributions with radial distance away from the jet centerline. Thus, the density distribution in the jet is given by:

$$g_{jet}(x, z, z_0) = \exp\left(-\frac{(z - z_0)^2}{2\sigma_{jet,\rho}^2(x)}\right). \tag{30}$$

where $\sigma_{jet,\rho}$ is the jet standard deviation (a measure of jet width) based on density. Similarly, measurements by Hinze and Van Der Hegge Zijnen (1949) and others (Wynanski and Fiedler (1969), Chen1980) show that axial velocities also follow Gaussian distributions about the jet axis. Therefore, the velocity distribution in the jet is given by:

$$u_c(x, z, z_0) = U_{CL} \exp\left(-\frac{(z - z_0)^2}{2\sigma_{jet,u}^2(x)}\right), \tag{31}$$

where $\sigma_{jet,u}(x)$ is the jet standard deviation based on velocity and $U_{CL}(x)$ is the velocity distribution along the jet

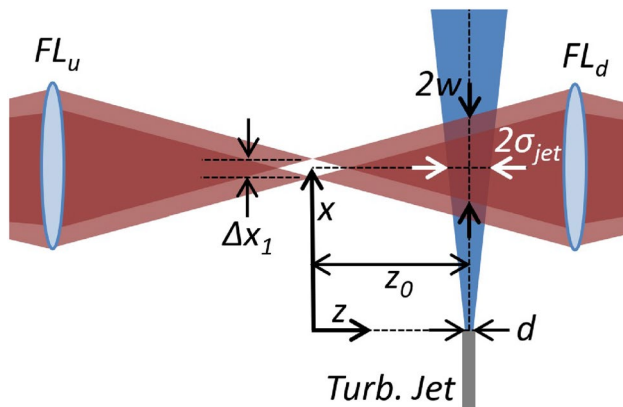


Fig. 5 Schematic of turbulent jet in relation to FLDI beams

center line. Hinze’s measurements showed that the spreading angle is $\sigma_{jet,\rho}(x) = 0.080x$ and $\sigma_{jet,u}(x) = 0.075x$ in the $Re_d = 6.7 \times 10^4$ turbulent jet. The jet centerline velocity distribution is found using Witze’s velocity decay model (Witze 1974), which is based on historical pitot and hot-wire measurements. This model is expressed as

$$U_{CL}(x) = 1 - \exp\left(-\frac{1}{\alpha(x/d) - X_c}\right), \tag{32}$$

where X_c , a universal parameter describing core length, takes a value of 0.7 and α , a parameter describing decay rate based on jet exit Mach number and ratio of jet exit density to ambient density, takes a value of 0.13 for a Mach number of 0.96 and a density ratio of 0.84 (Witze 1974).

H_{jet} is evaluated by substituting Eqs. 31, 19, 26, and 30 into Eq. 29 and evaluating the integral numerically. The result is a function of $\lambda_0, w_0, \Delta x_1, z_0, x$, and f . Rearranging Eq. 27 gives an expression for the average density fluctuation spectrum in the jet at any downstream distance in terms of the measured phase difference $\Delta\phi$, the parameters of the instrument, the downstream distance in the jet (x) and the disturbance frequency (f):

$$A_{jet}(f, x) = \frac{\lambda_0 \rho_s}{4\pi\beta} \frac{\mathcal{F}[\Delta\phi]}{H_{jet}(\lambda_0, w_0, \Delta x_1, z_0, x, f)} \tag{33}$$

$A_{jet}(f, x)$ is the amplitude of the density fluctuation at frequency f . It may also be thought of as the spectrum measured by an ‘ideal’ LDI with a beam radius and beam separation of zero. If the density model (10) is correct, $A_{jet}(f, x)$ measured in the turbulent jet using Eq. 33 should be independent of instrument parameters like Δx_1 and $w(z)$ as well as position of the jet along the optical axis, z_0 (although the uncertainty in $A_{jet}(f, x)$ may not be). We will check to see if this is the case in a later section.

2.2 Two-point FLDI (2pFLDI)

Fig. 6 is a schematic illustration of 2pFLDI. An additional birefringent prism (P_2) splits the beam not far from the laser head to create a second FLDI ‘channel’. The rest of the instrument uses the same optics as the single FLDI plus a polarizer (Pol_2) (or a quarter-wave-plate rotated at 45° or a half-wave plate rotated at 22.5°) that is needed to reset the polarization before the up-beam prism ($P1_u$). P_2 can also be placed down-beam of the objective lens (OL) or replaced with a Koester prism (Jewell et al. 2019), Nomarski prism (Bathel et al. 2020), or diffracting optic (Gragston et al. 2021b). P_2 is placed up-beam of OL in this work in order to accommodate existing resources in the lab. For future 2pFLDI setups, the authors recommend designing the set-up with a Nomarski prism (Bathel et al. 2020), with P_2 as close to $P1_u$ as possible (with room for

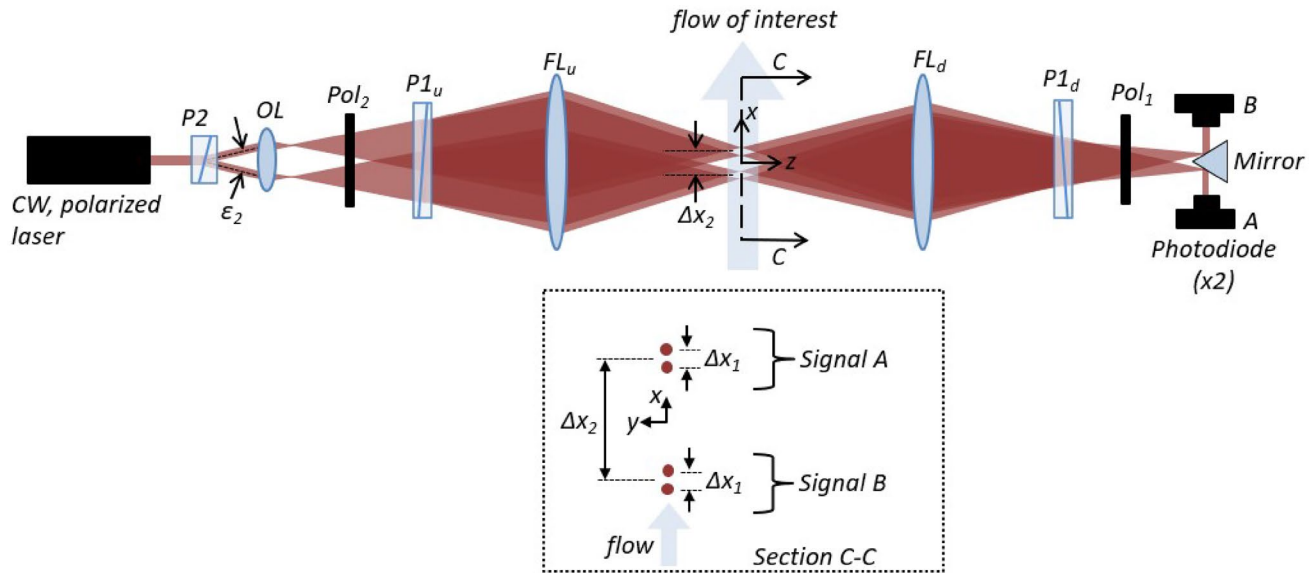


Fig. 6 Schematic illustration of a Two-Point Focused Laser Differential Interferometer. (P2) birefringent prism with splitting angle (ϵ_2), (Δx_2) separation between beam pairs

the polarizer/wave plate in between), or by following the detailed procedure outlined by Neet et al. (2021).

The desired result is a set of beam pairs that come to focus along one line on the x-axis as shown in Section C-C of Fig. 6. Down-beam of the focal volumes, another optical element like a mirror is required to divert the two FLDI beams to separate photodetectors. We now have two independent FLDI signals A & B with phase differences $\Delta\phi_A(t)$ and $\Delta\phi_B(t)$ respectively. The beam pair foci are separated by a distance (Δx_2).

The normalized cross correlation between signals A & B is given by:

$$R_{AB}(\Delta t) = \int_0^T \frac{\Delta\phi_A(t)\Delta\phi_B(t + \Delta t)}{\sqrt{|\Delta\phi_A|^2}\sqrt{|\Delta\phi_B|^2}} dt, \tag{34}$$

where Δt is the time shift between signals. In general, convection velocities are found from cross (also called space-time) correlations between signals in turbulent flow (Wallace 2014). The convective velocity (u_c , in the direction of the x-axis) is found by dividing the beam separation by the time shift which maximizes the cross-correlation:

$$\langle u_c \rangle = \frac{\Delta x_2}{\Delta t[\max(R_{AB})]}. \tag{35}$$

The use of angled brackets, $\langle \rangle$, emphasizes that this measurement is a time-averaged velocity over the sample period T .

Taylor (1938) famously hypothesized and later showed that turbulent structures in flows with low turbulence intensity ($u'/U \ll 1$) and negligible mean shear

($k_x U \gg \frac{dU}{dy}$) (Lin 1953) such as the those produced behind a grid in a wind tunnel convect with the mean flow velocity such that $u_c = U$ regardless of probe separation, Δx_2 . In shear-generated turbulent flows like those found in boundary layers and jets, the convection velocity is more complex and varies with probe separation as well as turbulent length and time scales (Favre et al. 1967; Kolpin 1964). Wills (1964) discusses the ambiguity of defining a convection velocity in shear flows and suggests that either a wavenumber-dependant velocity, $u_c(k_x)$, or a frequency-dependant velocity, $u_c(f)$, is more physically meaningful. The 2pFLDI can measure frequency-dependant convection velocity either by bandpass filtering signals A and B (Ceruzzi et al. 2020) or by computing the cross-spectrum of A and B (Gillespie et al. 2021). The cross power spectral density is given by the Fourier transform of the cross correlation:

$$\Gamma_{AB}(f) = \int_{-\infty}^{\infty} R_{AB}(\Delta t)e^{-2\pi if\Delta t} d\Delta t. \tag{36}$$

The phase of the the cross spectrum is given by

$$\phi_{\Gamma}(f) = \arctan \left[\frac{\mathcal{I}(\Gamma_{AB})}{\mathcal{R}(\Gamma_{AB})} \right], \tag{37}$$

where \mathcal{I} and \mathcal{R} denote the imaginary and real parts, respectively. The frequency-dependant convection velocity is given by:

$$u_c(f) = \frac{2\pi\Delta x_2 f}{\phi_\Gamma} \tag{38}$$

Both methods (Eqs. 35 and 38) are used here to compare $\langle u_c \rangle$ and $u_c(f)$ respectively.

3 Experimental set-up and methods

3.1 Turbulent air jet

The flow studied in this work is produced by the round jet illustrated in Fig. 7. Compressed air enters a 48 mm (1.9”) ID plenum and accelerates through a smoothly converging nozzle with an exit diameter of 3.175 mm (0.125”). A diaphragm-type pressure regulator equipped with a strainer to trap debris and a Bourdon tube gauge (accuracy $\pm 2\%$) maintains a constant pressure of $12 \pm$ lpsig (26.7 psia, 1.8 atm, 184 kPa) in the plenum. This pressure is chosen to maximize Reynolds number while avoiding supersonic flow at the jet exit. The resulting nozzle exit velocity, Mach number, and Reynolds number based on jet diameter are 306 ± 7 m/s, 0.96 ± 0.01 , and $8.55 \pm 0.34 \times 10^4$ respectively assuming isentropic flow through the nozzle.

The air jet is oriented vertically and mounted on a motorized 3-axis Velmex Bi-Slide stage. This enables the jet to be

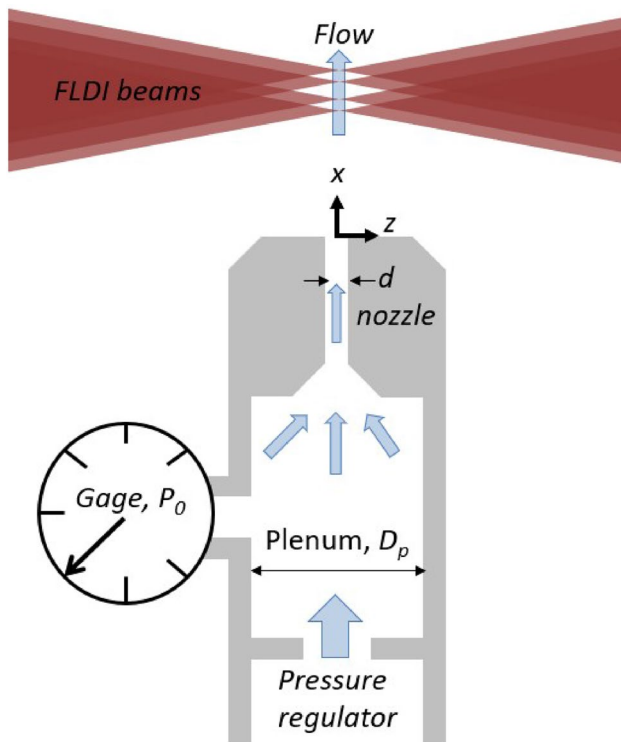


Fig. 7 Illustration of air jet cross-section and experimental set-up. $d = 3.2$ mm(0.125”), $D_p = 48$ mm(1.9”), $P_0 = 1.8$ atm(12psig)

moved in three dimensions through the FLDI measurement volume which remains fixed. The x-axis is the centerline of the jet and parallel to the line connecting the centers of the four focal volumes. Positive x points up with respect to the laboratory and downstream with respect to the jet flow. The y and z axes are perpendicular to the x-axis with z parallel to the FLDI optical axis and y perpendicular.

3.2 FLDI Parameters

The FLDI constructed in this work uses a 0.8mW HeNe laser, N-BK7 lenses (OL, FL) from ThorLabs, Polarizers from ThorLabs (LPVISE100-A), and a $13\text{mm}^2, 14\text{ns}$ rise-time photodetector from ThorLabs (DET36A). For beam splitting/recombining ($P1_u$ & $P1_d$) we alternate between Wollaston prisms from United Crystals with a splitting angle of 4arcmin and custom made stress-birefringent ‘Sanderson’ prisms (Sanderson 2005; Fulghum 2014; Settles and Fulghum 2016) which allow splitting angles below 4arcmins. The 2pFLDI uses much of the same equipment as the single point FLDI. All beam splitting is accomplished with Wollaston prisms ($P1_u, P1_d$ & $P2$) from United Crystals and the optical axis length of the set-up is shortened to increase the convergence angle of the beam thereby improving rejection of disturbances away from the focus. P2 is located 15 mm up-beam of OL. Table 1 gives all relevant parameters for both set-ups.

3.3 Data reduction

The photodetector signals are terminated at 1 k Ω and digitized by a 16-bit Picoscope 5444A. The sampling frequency varies but is always between 1 and 4 MHz. Raw voltages are downloaded from the scope and processed using MATLAB. Voltage is converted to phase difference using Eq. 8.

Fourier transforming the phase difference fluctuations is required for the signal analysis described in Sect. 2. This is

Table 1 Parameters of FDLI used in work. See Fig. 3 and Fig. 6 for reference. w is the Gaussian beam radius parameter (Siegman 1986)

Parameter	FLDI	2pFLDI	Units
f_{OL}	15	15	mm
f_{FL}	260	125	mm
ϵ_1	0.5, 1.4, 4	4	arcmin
Δx_1	35, 100, 290	145	μm
$D_{FL}(2w)$	28	25	mm
L_i	508	170	mm
w_0	7.3	3.0	μm
λ_0	632.8	632.8	nm
ϵ_2	–	10	deg
Δx_2	–	1.2	mm

accomplished by taking the square-root of the power spectral density, which we estimate using Welch’s method (Welch 1967) via the MATLAB function `pwelch` with 3.3ms Hamming windows and 50% overlap.

For 2pFLDI, the MATLAB function `xcorr` computes the normalized cross-correlation (Eq. 34) between two signals. If the correlation peak is less than 0.1, the signals are considered noise-dominated and velocity is not computed. Otherwise, the index of maximum correlation divided by the sampling frequency gives the time lag (Δt) between the two signals enabling the disturbance velocity, $\langle u_c \rangle$, to be calculated using Eq. 35. For frequency-dependant velocities, the MATLAB function `cpsd` computes the cross-spectrum (Eq. 36). Like the power spectrum, this method also uses Welch’s method with 3.3ms windows and 50% overlap. The cross spectra phase (Eq. 37) can only take values from $-\pi$ to π . This will give accurate velocity measurements for $k_x < \pi/\Delta x_2$. For wavenumbers above this, phase ambiguity will occur. This is corrected by assuming the velocity variation with wavenumber is smooth and continuous. In practice, as frequency increases (hence wavenumber increases), 2π is added to the phase every time there is a discontinuous jump from π to $-\pi$. This process is outlined with more detail by Buxton et al. (2013).

3.4 Adjustment and measurement of beam separation Δx_1

Beam separation is varied by replacing the Wollaston prisms (whose splitting angles are fixed) with variable-angle stress-birefringent Sanderson Prisms (Sanderson 2005). FLDI measurements are made using three values of Δx_1 . Beam separation is measured by imaging the beams at the focus using a beam profiler camera (Newport LBP2) with a $3.69\mu\text{m} \times 3.69\mu\text{m}$ pixel size. Sample images are presented in Fig. 8. Two Gaussian distributions (one for each beam) are fit to the intensity distributions in the x-y plane. The difference between the centers of each Gaussian distribution is the beam separation. The uncertainty is approximately equal to the pixel size ($3.7\mu\text{m}$) resulting in an uncertainty of $\sim 10\%$ for the smallest beam separation. Note that the Wollaston prism ($\Delta x_1 = 290\mu\text{m}$) produces beams that are much more uniform/Gaussian-like than those produced by the Sanderson prism ($\Delta x_1 = 100\mu\text{m}$ and $\Delta x_1 = 35\mu\text{m}$).

3.5 Measurement of focal spot radius, w_0

An accurate measure of the beam spot size at the focus is needed to compute the FLDI sensitivity function as well as the spot size at any z-location via. Equation 25. Unfortunately, the pixel size of the beam profiler camera is too large to directly measure the spot size at the focus. However, since the beam diameter increases linearly with z far

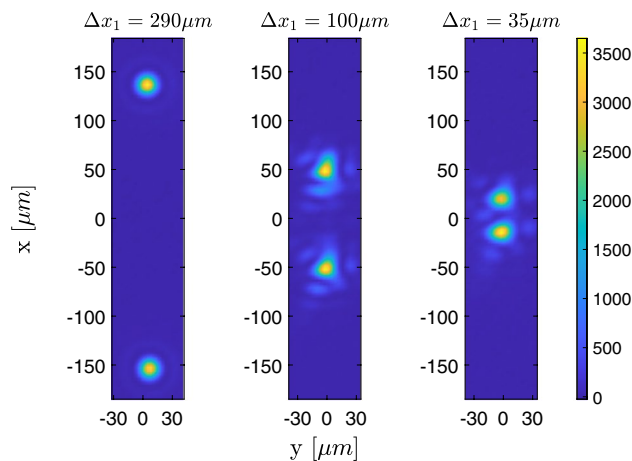


Fig. 8 Comparison of beam profiles at the focus for three setups. $\Delta x_1 = 290\mu\text{m}$ is produced using the Wollaston prism. The other two beam spacings are produced using the Sanderson prism

from $z = 0$, we can use the beam profiler camera to measure $w(z)$ at seven non-uniformly spaced distances ranging from $z = 3.175\text{mm}$ to $z = 25.4\text{mm}$ and infer the beam radius at the focus (w_0) using Eq. 39 with $\lambda_0 = 633\text{nm}$.

$$w(z) \approx \frac{\lambda_0}{\pi w_0} z, \tag{39}$$

Examples of beam intensity profiles measured at three locations are presented in Fig. 9. Gaussian intensity distributions fit to each image are used to find the Gaussian beam radius parameter w where $w = 2\sigma$ and σ is the standard deviation of the Gaussian distribution (Siegman 1986). Note that the up beam prism is temporarily removed so a single beam is being measured, not two beams split by $290\mu\text{m}$ as in the actual setup. This makes no difference since the divergence angles of the two beams are the same as that of the original.

The results of the beam radius parameter measurements are plotted in Fig. 10. A linear fit correlates the measurements extremely well ($R^2 = 0.999$) and enables us to determine that the beam radius at the focus is $7.3 \pm 0.5\mu\text{m}$ ($\sim 7\%$).

4 FLDI results

4.1 Sensitivity to beam separation (Δx_1)

As its name suggests, the differential interferometer performs a finite difference on the index of refraction field. Dividing the signal by the beam separation (Δx_1) yields a signal proportional to the first order approximation of the density gradient. However, the instrument is also sensitive to wavenumber as explained in the previous section and by

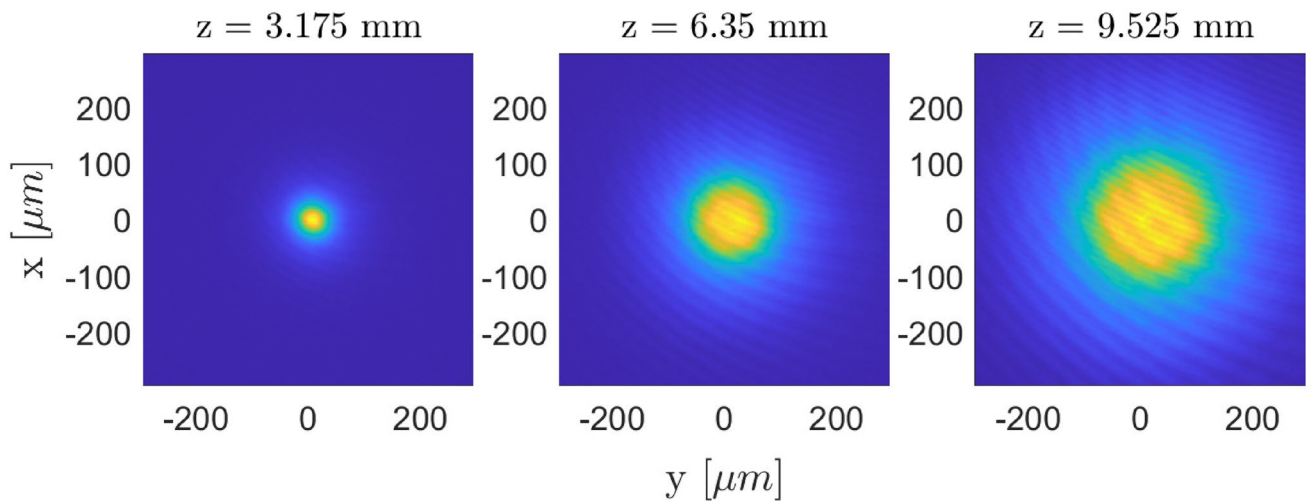


Fig. 9 Beam intensity profiles along the z axis

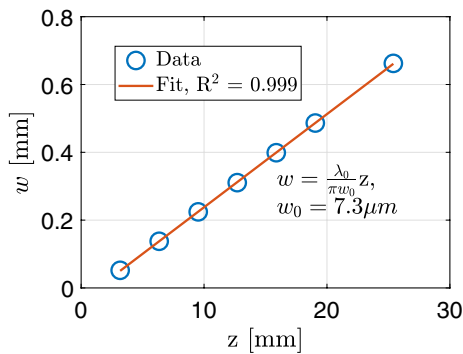


Fig. 10 Sample measurements of the beam radius parameter at various points along the z axis with the fit used to determine w_0 , the beam radius at the focus

Parziale in much of his FLDI work (see for example Fig. 3 in Parziale et al. (2014)). This is accounted for here using a transfer function developed for sinusoidal variations (Eq. 19). Lawson et al. (2020) uses FLDI simulations to illustrate the effect of varying the beam separation when the disturbance field is static. They note that the signal magnitude increases and x-axis spatial resolution decreases as Δx_1 increases. These effects are qualitatively consistent with those predicted by $H_{\Delta x}$ (Eq. 19). The question we seek to answer in this section is to what extent Eq. 19 models the FLDI’s response to the dynamic, turbulent flow field produced by the jet.

In each experiment, the turbulent jet is aligned with the beam’s focus ($z_0 = 0$) and is translated in the streamwise direction along the x-axis. Measurements are made at five uniformly spaced locations from $x/d=5$ to $x/d=25$ and the FLDI signal is sampled for 20ms at 2MHz at each. Measurements of signal strength (which is proportional

to phase difference) at $x/d=15, 20$ and 25 are presented in Fig. 11 for three different values of Δx_1 . The results show that the phase difference increases with beam separation for low frequencies. This can be explained by thinking of the signal magnitude divided by the beam separation as proportional to the density gradient, i.e. $\Delta\phi/\Delta x_1 \propto \partial\rho/\partial x$. Thus for a fixed density gradient magnitude, phase difference will increase linearly with beam separation. We observe this trend for frequencies below $\sim 10^5 Hz$. Above $\sim 10^5 Hz$ phase difference decreases with frequency. This decline is more prominent for the largest beam separation, $\Delta x_1 = 290\mu m$. This behavior represents spatial filtering of wavenumbers which exceed $\pi/\Delta x_1$. This disturbance scale corresponds to a range of frequencies, because the convection velocity varies through the jet. Note that spectral content below $\Delta\phi \sim 2 \times 10^{-6}$ radians is assumed to be noise and is removed prior to subsequent data processing. This “noise floor” is evident at the highest frequencies in Fig. 11 where the spectra flatten and coalesce with spectra measured when the flow is off (not shown here).

Figure 12 shows the overall transfer function H_{jet} as a function of frequency and beam spacing for the measurements presented in Fig. 11. H_{jet} is calculated by plugging Eqs. 30 and 31 into Eq. 29 and integrating numerically, using trapezoidal integration (MATLAB function trapz) with 1001 linear-spaced z values between $z_0 - 4\sigma_{jet,\rho}$ and $z_0 + 4\sigma_{jet,\rho}$. The filtering behavior is apparent as H_{jet} increases linearly with frequency until the frequency of the disturbance approaches the point of maximum sensitivity. The true average density fluctuation spectrum is recovered by dividing the signal by H_{jet} as per Eq. 33. The results are presented in Fig. 13. The collapse of all spectra indicates H_{jet} (Eq. 29) and thus $H_{\Delta x}$ (Eq. 19) is a good model for the effects of beam separation on this flow field. While results from

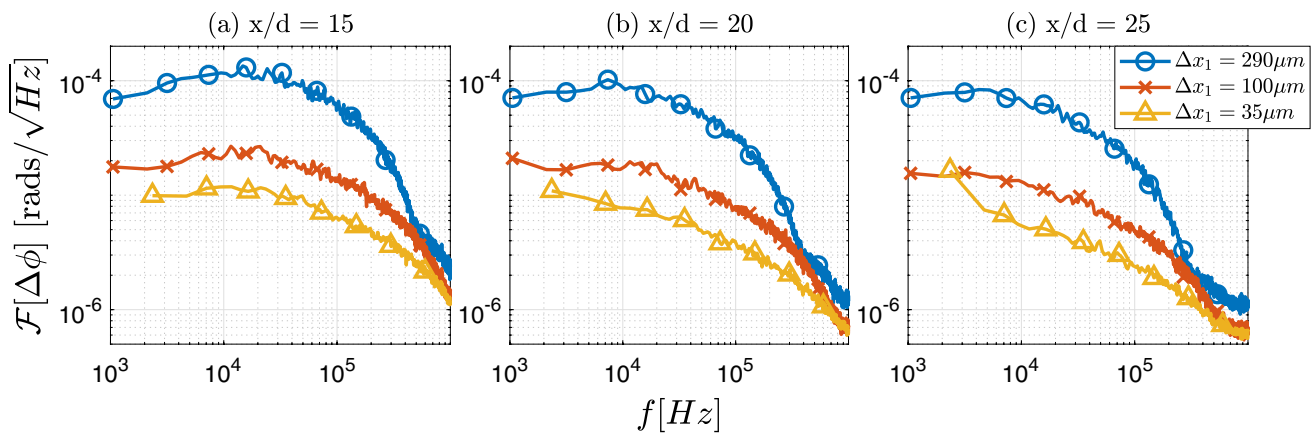


Fig. 11 Raw FLDI phase difference spectra for three beam separations acquired at jet centerline ($y/d = 0$) and instrument focus ($z_0/d = 0$)

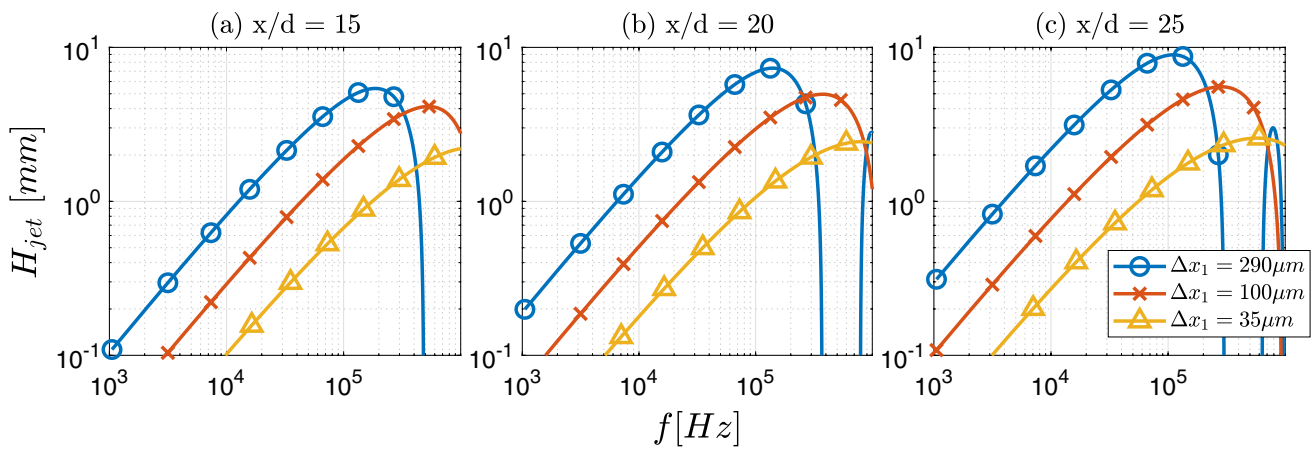


Fig. 12 FLDI sensitivity function to the jet (Eq. 29) for three beam separations at jet centerline ($y/d = 0$) and instrument focus ($z_0/d = 0$). $w_0 = 7.3 \mu\text{m}$, and $\lambda_o = 632.8 \text{nm}$

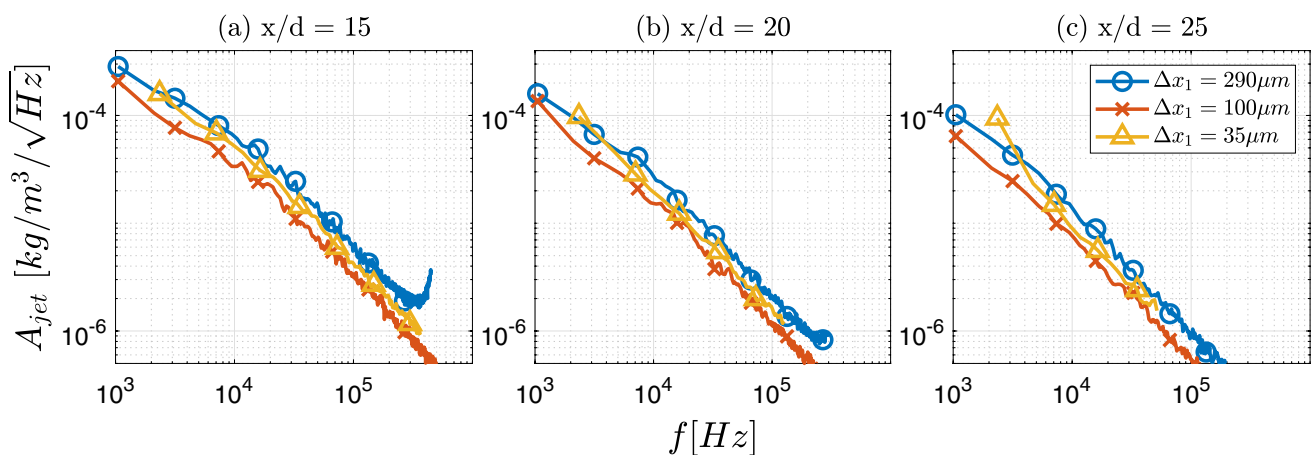


Fig. 13 Average amplitude spectra interrogated by FLDI, found from Eq. 33. Measurements are acquired at the jet centerline ($y/d = 0$) and the instrument focus ($z_0/d = 0$)

measurements at only three locations are presented here, similar collapses are observed at all jet locations.

To quantify the model’s accuracy, we compute the difference between amplitude spectra (A_{jet}) measured at the three beam separations and normalize by the value from $\Delta x_1 = 35\mu m$. This is plotted in Fig. 14. These values provide a measure of the model’s (Eq. 33) accuracy. Figure 14 shows that the amplitudes recovered from $\Delta x_1 = 100\mu m$ & $35\mu m$ differ by $\sim 25\%$ over the band $5kHz < f < 200kHz$ while the amplitudes recovered from $\Delta x_1 = 290\mu m$ & $35\mu m$ differ by $\sim 50\%$ over the same band. The effect of beam separation appears to be independent of x/d .

We will first check to see if these discrepancies can be explained by quantifiable uncertainties in the experiment. The uncertainty in the jet’s mean density is $\sim 2\%$ based on the accuracy/repeatability of the gauge measuring plenum pressure described in Sect. 3.1. The precision of the 3-axis stage exceeds $6\mu m$, thus the uncertainty associated with location of the FLDI probe is considered negligible. The uncertainty in the beam separation is $\sim 10\%$ at most (see Sect. 3.4). For $f \ll \frac{u_c}{2\Delta x_1}$ ($f < 100kHz$ in this work), this uncertainty translates directly to a $\sim 10\%$ uncertainty in amplitude per the beam separation transfer function, $H_{\Delta x}$. None of the above explain errors on the order of 50%. Uncertainties which we are unable to quantify include noise introduced by different optical components, primarily the beam splitting prisms which vary between experiments, and error introduced by beams which deviate from Gaussian profiles, as is observed in Fig. 8. We note these experiments were conducted over the course of two days as changing Δx_1 required that major optical components be exchanged and the instrument be re-calibrated. We also note that experiments with $\Delta x_1 = 100\mu m$ & $35\mu m$ used the same type of beam splitting prism (Sanderson prism) while experiments with $\Delta x_1 = 290\mu m$ used the traditional Wollaston prism.

In the next section we show that errors associated with varying the local beam diameter are significantly smaller ($\sim 10 - 20\%$). This, as well as the fact that there is no consistent trend in the difference between amplitude spectra as Δx_1 is increased, suggests that the differences observed here are mainly due to changes in the optical setup required to change Δx_1 and not Δx_1 itself or discrepancies between our model (Eq. 10) and the true density gradient fluctuations in the flow.

4.2 Sensitivity to position along the optical axis (z)

In this section, we investigate how FLDI sensitivity changes along the optical axis (z-direction) which is important for evaluating the improvement in spatial resolution brought about by focusing. A single beam separation of $\Delta x_1 = 290\mu m$ (which provides the largest overall signal strength) is considered in order to isolate the effect of z. The turbulent jet is translated in the streamwise (x-axis) and spanwise (z-axis) directions. Data are collected at ten uniformly spaced x-locations ranging from $x/d=5$ to $x/d=50$ and 21 non-uniformly spaced locations in the z-direction ranging from $z_0/d = -5$ ($z_0 = -15.9mm$) to $z_0/d = 70$ ($z_0 = 222.2mm$). At each location, the FLDI signal is sampled for 400ms at 1MHz. A sketch of the experiment is shown in Fig. 5.

Phase difference spectra are presented in Fig. 15 for eighteen measurement locations ($x/d=20, 30, 40$ and six z_0 locations). The results show that signal strength decreases as the jet moves away from the instrument’s focus (increasing z_0). Higher frequencies are more strongly affected by the movement of the jet away from the focus because these frequencies correspond to small wavelength disturbances which are spatially averaged to a greater extent than relatively larger wavelengths (lower frequencies). Figure 16 shows the values of H_{jet} corresponding to the eighteen measurement locations plotted in Fig. 15. Prior to calculating H_{jet} , frequencies

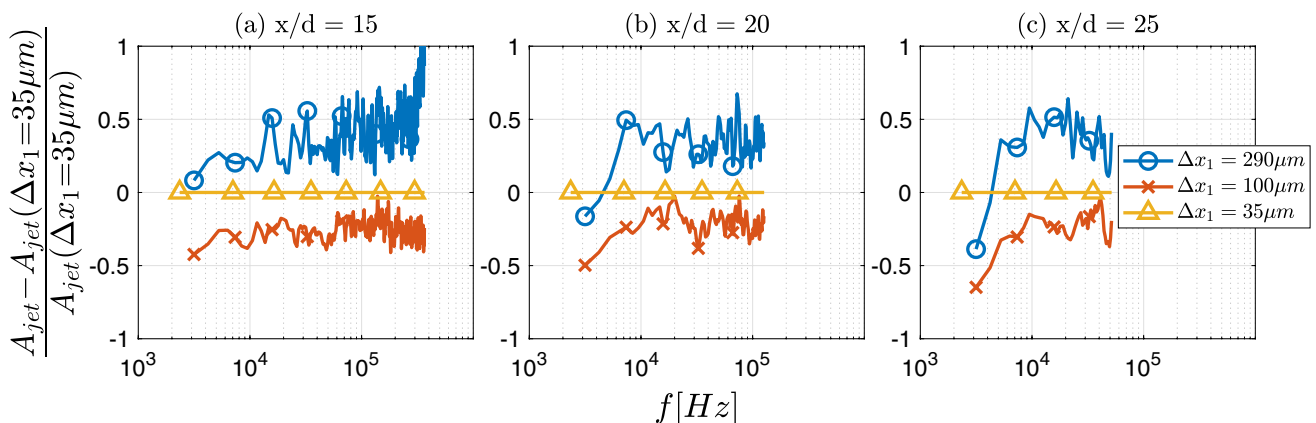


Fig. 14 Difference between amplitude spectra recovered by Eq. 33 for three beam separations, normalized by amplitude from $\Delta x_1 = 35\mu m$. Measurements are acquired at the jet centerline ($y/d = 0$) and the instrument focus ($z_0/d = 0$)

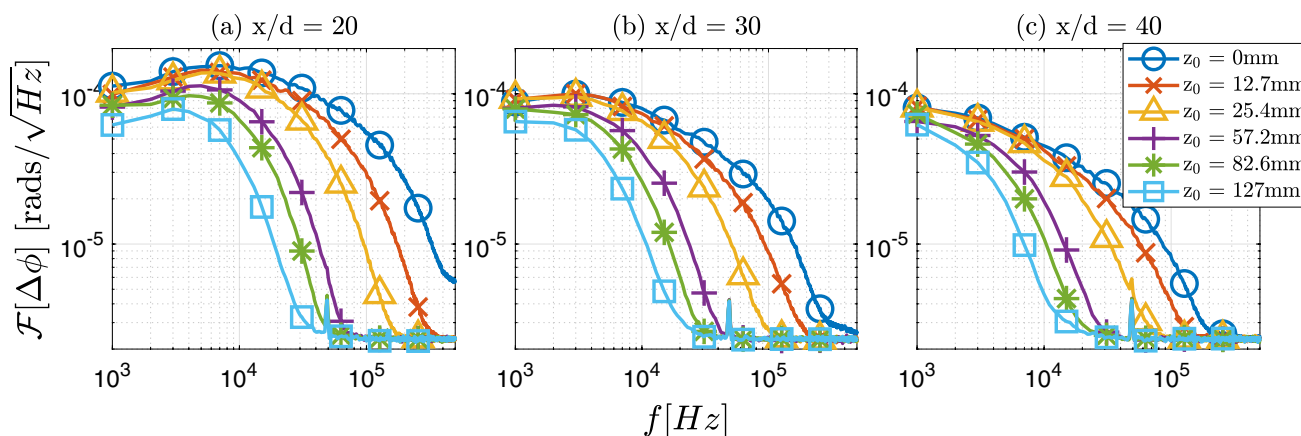


Fig. 15 Raw FLDI phase difference spectra acquired at jet centerline ($y/d = 0$) for six jet positions along the optical axis (z_0)

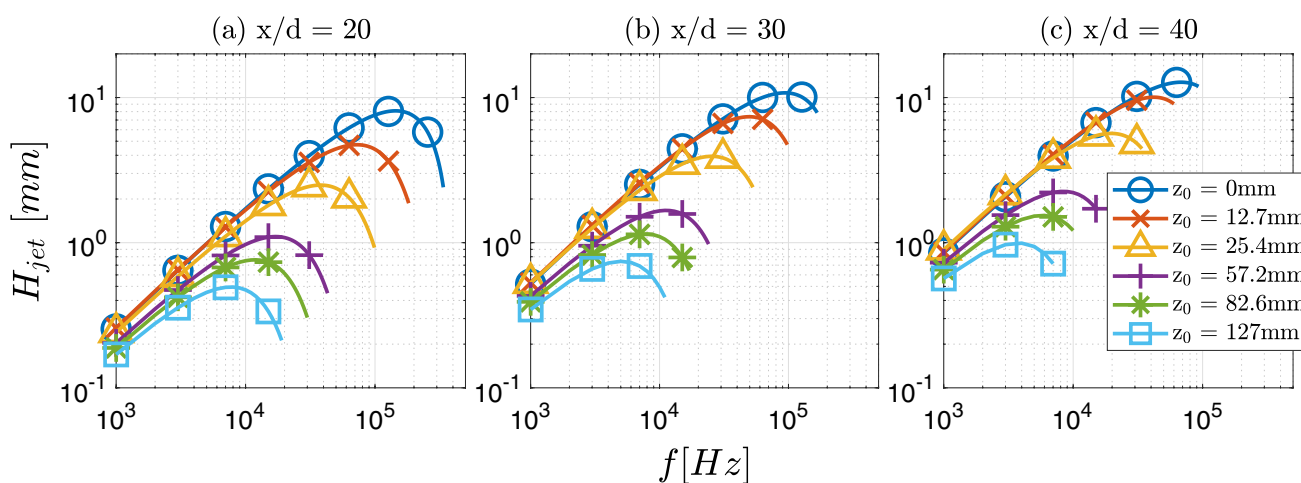


Fig. 16 FLDI sensitivity function to the jet (Eq. 29) at jet centerline ($y/d = 0$) for six jet positions along the optical axis (z_0)

which contain spectral content below $\Delta\phi \sim 2 \times 10^{-6}$ radians are assumed to be noise and removed. These curves predict the instrument’s sensitivity to the jet at different values of z_0 . As in the previous section, we use Eq. 33 to recover the true average density fluctuation spectra. The results, presented in Fig. 17, show that measurements at all z -locations collapse indicating that H_{jet} has correctly captured the effect of position along the optical axis. While data for only three streamwise and six z -axis positions are presented here - for clarity - collapse is observed for all frequencies measured ($f > 500\text{Hz}$) and for all streamwise positions above $x/d=15$. Below $x/d=15$, the assumption that disturbances are normally distributed breaks down and the model is not expected to work.

Once again, we assess the model’s effectiveness - i.e. its ability to predict and compensate for the effects of disturbances away from the focal volume - by computing the difference between amplitudes recovered for the various

z -axis positions and the amplitude at the instrument’s focus ($z_0 = 0$) as illustrated in Fig. 18. The results show that the error is less than $\pm 20\%$ for almost all frequencies and cases presented here. The error only exceeds 20% for the higher frequencies at $x/d = 20$. This is the result of the noise floor which we were not able to remove fully. In fact, for $x/d=30$ & 40 and $f < 10\text{kHz}$, the error is below $\pm 10\%$. This is a significant improvement over the error associated with varying the beam separation (25–50%).

The quantifiable uncertainties in these experiments are the jet mean conditions ($\sim 2\%$) and the local beam radius $\sim 7\%$. All experiments are conducted using the same optical components and each spectrum is collected within the same ~ 30 minute time period. Therefore, uncertainties associated with transient changes in room conditions, optical, and electronic noise are expected to be much smaller than those in the beam separation tests. This, along with the fact that the optical configuration remained unchanged, could explain

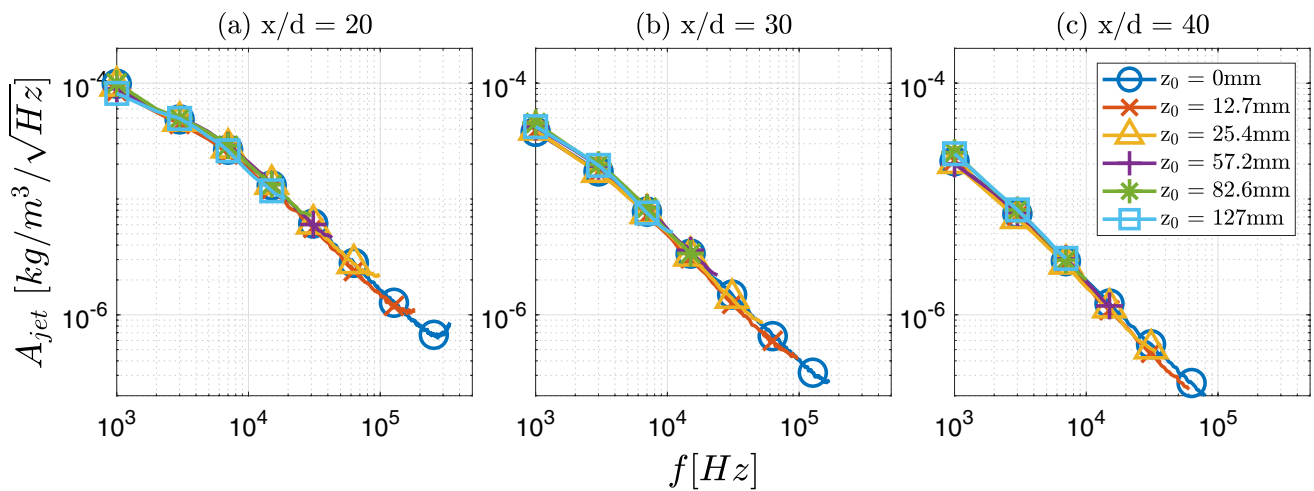


Fig. 17 Average amplitude spectra interrogated by FLDI, found from Eq. 33, for jet centerline ($y/d = 0$) and for six jet positions along the optical axis (z_0)

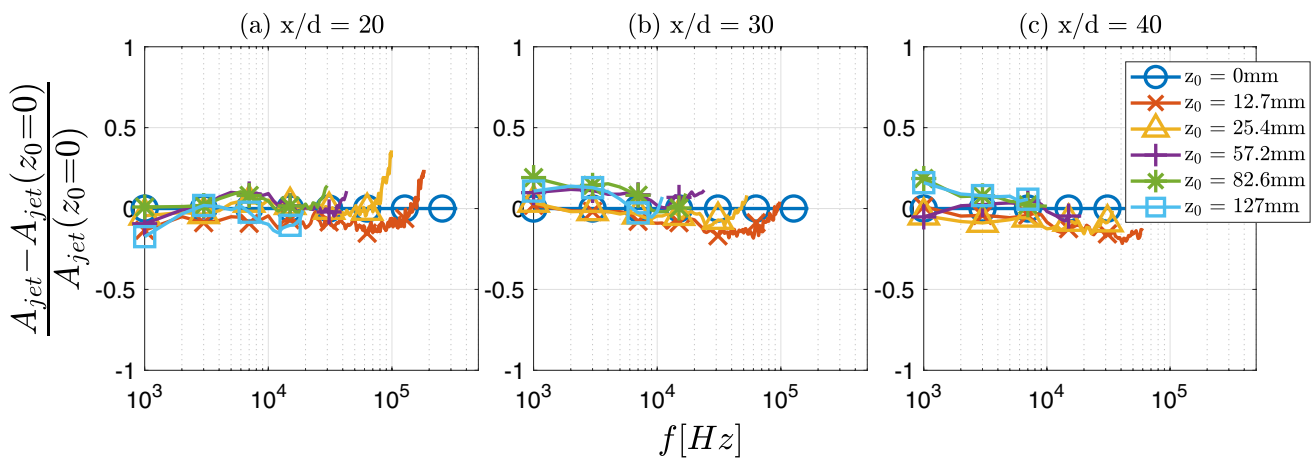


Fig. 18 Difference between amplitude spectra recovered for six jet positions along the optical axis (z_0), normalized by amplitude at $z_0 = 0$

the smaller variations observed here compared to the beam separation experiments.

4.3 Sensitivity to simultaneous changes in Δx_1 and z_0

To comprehensively validate our model of FLDI sensitivity, we investigate the ability to recover the averaged density fluctuation when both beam separation (Δx_1) and jet position (z_0) are varied. The turbulent jet is translated in both the streamwise (x) and spanwise (z) directions and probed using three different FLDI setups: ($\Delta x_1 = 35, 100, 290 \mu m$). Measurements are made at five uniformly spaced locations in the x -direction ranging from $x/d=5$ to $x/d=25$ and 21 non-uniformly spaced locations in the z -direction ranging from $z_0 = -15.9 mm$ to $z_0 = 222.2 mm$. Phase difference, H_{jet} , average

amplitude spectra, and normalized-amplitude-difference are plotted in Fig. 19 for measurements made at $x/d=20$ and $y/d = 0$. The amplitude differences presented in Fig. 19.d are normalized by the amplitudes associated with $\Delta x_1 = 35 \mu m$, $z_0 = 0$. These differences are below $< 50\%$ over the frequency range $4 - 100 kHz$ with the exception of those collected with $\Delta x_1 = 290 \mu m$. As shown in the previous two sections, there appear to be larger differences between experiments with different beam separations than between experiments with different jet locations. This is probably because changing the beam separation required changing optical components and collecting data over multiple days whereas translating the jet could be accomplished quickly and without altering the optics.

$$x/d = 20$$

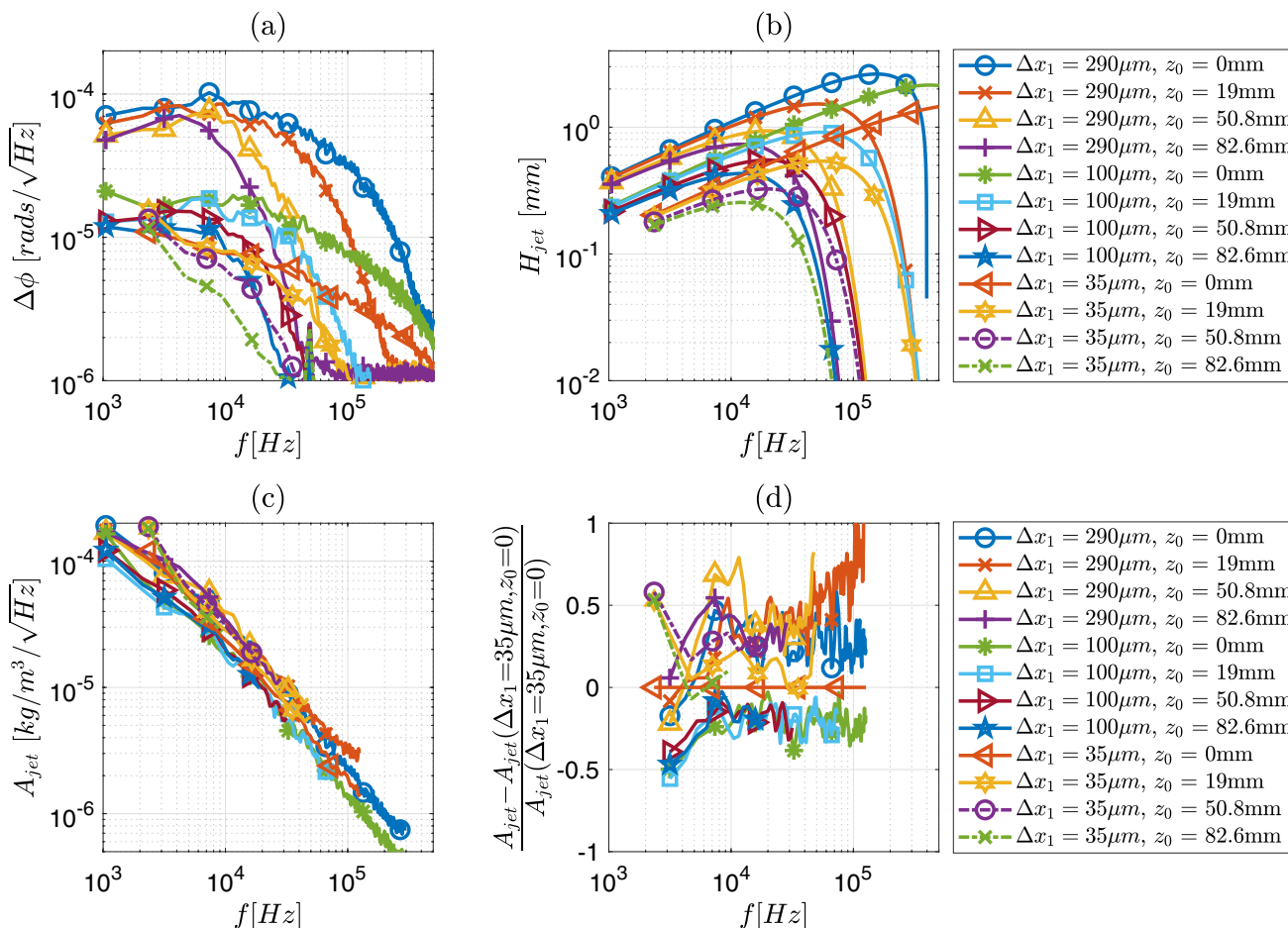


Fig. 19 (a) Phase difference spectra, (b) sensitivity functions, (c) average amplitude spectra, and (d) amplitude difference normalized by amplitude at $\Delta x_1 = 35\mu m, z_0 = 0$. All data collected at $x/d = 20, y/d = 0$

5 2pFLDI results

This section demonstrates 2pFLDI: measurements of disturbance velocity using two closely spaced FLDI measurement volumes. Recall that 2pFLDI theory is explained in Sect. 2.2. Also note that the geometry of the single FLDI setup is slightly different than the FLDI setups used to obtain the previous results as is explained in Sect. 3.

5.1 Measuring beam-pair separation, Δx_2

The beam pair separation (Δx_2) can be estimated using paraxial ray-tracing (Poon and Kim 2006) or ray-tracing software such as Code-V or ZEMAX but it is more accurate to measure it. This is best accomplished using a beam profiler camera as done in Sect. 3.4. Unfortunately, this camera was not available when the 2pFLDI experiments were performed so the beam separation was determined by translating a knife-edge in the x-direction through the focal region

while measuring both detectors’ output voltage at 33 equally spaced points over 3.175 mm. Figure 20.a shows the results. The knife edge initially blocks both signals so the output voltages are both zero. As the knife edge is moved away, first detector A and then detector B are uncovered. Figure 20.b, shows the derivative of the signals dV/dx with respect to x . Gaussian functions are fit to the derivatives of each signal in order to reduce uncertainty in locating the peak. The distance between the Gaussian peaks is taken to be the beam spacing. The results show that $\Delta x_2 = 1.18 \pm 0.1 mm$.

5.2 Quantifying the depth of focus

Fig. 21 illustrates the sensitivity of the 2pFLDI in this work. Wavenumber and z are normalized by the jet diameter. Figure 21 shows that the instrument has maximum sensitivity to $k_x \sim 70/d$, which corresponds to wavelengths on the order of $300\mu m$. We define the depth of focus as the full-width-half-max (*FWHM*) of a horizontal slice of Fig. 21.

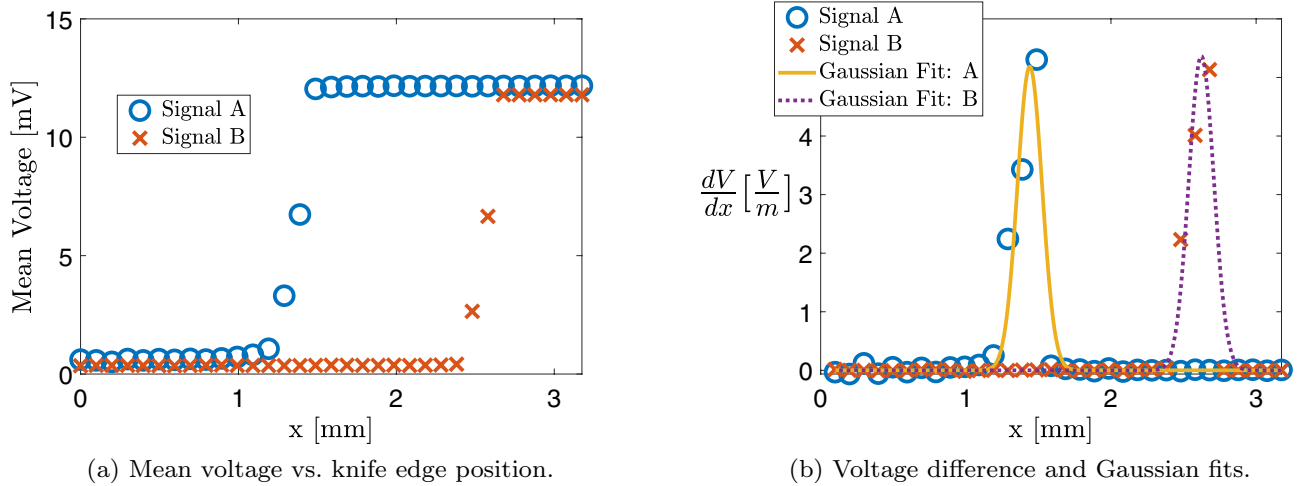


Fig. 20 Results from knife-edge test used to determine beam pair separation (Δx_2)

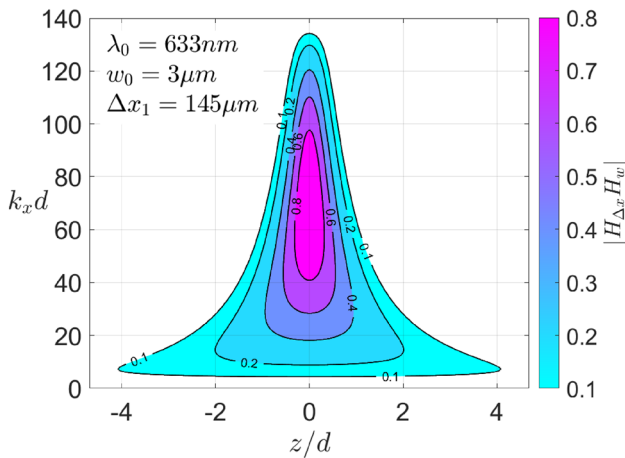


Fig. 21 Variation of the product of FLDI transfer functions $H_{\Delta x} H_w$ with wavenumber and z for $\lambda_0 = 633\text{nm}$, $w_0 = 3.0\mu\text{m}$, $\Delta x_1 = 145\mu\text{m}$

An analytical expression for the $FWHM$ can be developed by recognizing $H_{\Delta x}$ is independent of z and that the maximum value of H_w always occurs at $z = 0$ ie:

$$H_w(z_{1/2}) = \frac{1}{2} H_w(z = 0), \tag{40}$$

where H_w is given by Eq. 26. Solving for $z_{1/2}$ (or $FWHM$) gives:

$$FWHM = \frac{2\sqrt{8 \ln 2\pi w_0}}{\lambda_0 k_x}. \tag{41}$$

This is plotted against wavenumber in Fig. 22 where both $FWHM$ and k_x are made dimensionless using the jet diameter d . At $k_x d = 70$, the depth of focus is approximately one jet diameter (3.2mm). We expect the most energetic scales to

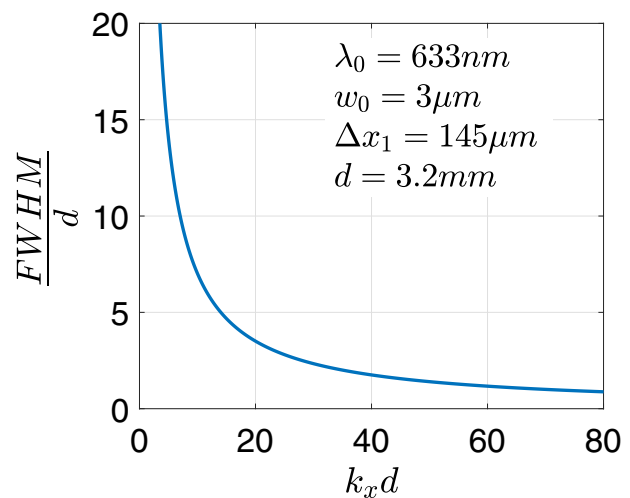


Fig. 22 Full-width half max of the the FLDI transfer functions (depth of focus) vs wavenumber for $\lambda_0 = 633\text{nm}$, $w_0 = 3.0\mu\text{m}$, $\Delta x_1 = 145\mu\text{m}$

be $k_x \sim 2\pi/d$. Figure 22 shows the depth of focus at these scales is $\sim 11d$ or 35mm . Thus, we should not expect the current version of the instrument to be able to resolve near field features of the jet.

The overall FLDI signal is the product of the instrument sensitivity, $H_{\Delta x} H_w$ and the amplitude of the disturbances, $A_{jet} g_{jet}$. Dividing this product by it's maximum value, which we call $[A_{jet} g_{jet} H_{\Delta x} H_w]_{norm}$, yields a dimensionless quantity that captures the variation in both the instrument's sensitivity and the magnitude of disturbances in the jet. This quantity is plotted in Fig. 23 for three downstream positions of the jet. It illustrates the function over which the instrument integrates to produce signal which, in turn, is used to compute the 2pFLDI convection velocity. Thus,

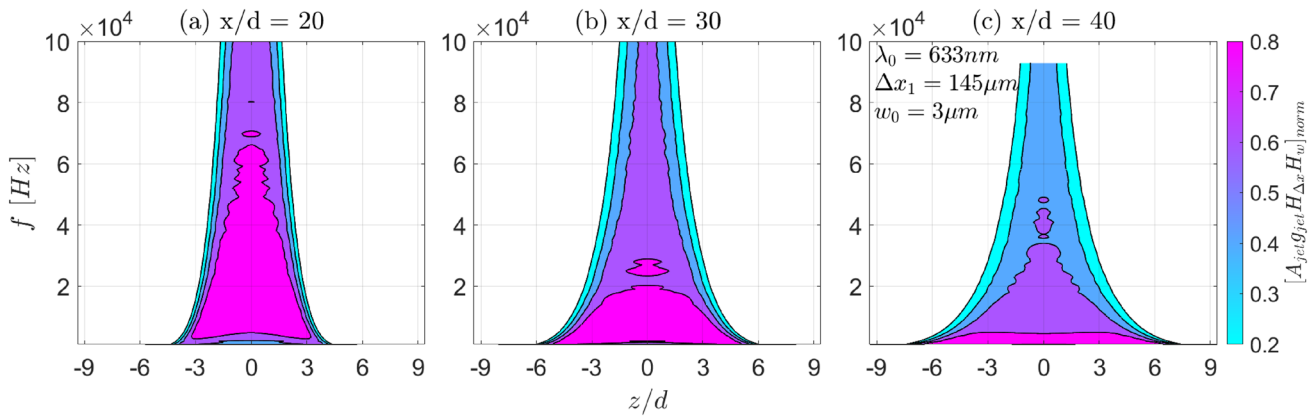


Fig. 23 Contribution of disturbances in jet to FLDI signal vs. frequency and dimensionless position along the z axis. Parameters of the FLDI are those used in the 2pFLDI set-up ($w_0 = 3\mu\text{m}$, $\Delta x_1 = 145\mu\text{m}$)

the curves plotted in Fig. 23 give a measure of the depth of focus and relative signal strength. The frequencies presented here represent a portion of the useful bandwidth $\sim 100\text{kHz}$ measured by our 2pFLDI in the jet. The values for A_{jet} are taken from previous measurements made at $\Delta x_1 = 290\mu\text{m}$ and $z_0 = 0$ (plotted in Fig. 17). This A_{jet} is chosen for its bandwidth ($> 100\text{kHz}$) and availability at $x/d > 25$. As discussed in the previous section, A_{jet} recovered from various FLDI set-ups and jet positions mostly agree within $\pm 50\%$ over $4 - 100\text{kHz}$. Thus, we take $\pm 50\%$ as the uncertainty in sensitivity to various frequencies reported here.

First, we note for all x/d that depth of focus decreases with increasing frequency. This is consistent with our basic understanding of the instrument: high wavenumber disturbances, which manifest as high frequency signals, are spatially filtered more rapidly than low wavenumber disturbances as one moves away from the focus. Signal strength drops with increasing frequency and as x/d increases. This has the effect of reducing the bandwidth which produces adequate signal to make a velocity measurement. Figure 23 also shows that the depth of focus at low frequencies ($f < 20\text{kHz}$) increases substantially with x whereas the depth of focus at high frequencies ($f > 40\text{kHz}$) varies little with downstream position. This is because the instrument’s sensitive region at low frequencies exceeds the width of disturbances in the jet and the jet broadens as one moves downstream. Note that $4\sigma_{jet,p} \approx 20\text{mm}$ at $x/d = 20$ and $\approx 40\text{mm}$ at $x/d = 40$. In contrast, the full-width-half-max of the sensitivity curve for $f = 80\text{kHz}$ spans $\sim 10\text{mm}$ for all x/d plotted here. We conclude that the 2pFLDI’s depth of focus is on the order of centimeters in scale. It can resolve the highest frequencies with $\sim 10\text{mm}$ depth of focus and the smallest frequencies with depth of focus on the order of the width of the jet, which grows from an initial 3.2mm diameter orifice at $x/d = 0$ to a span of $4\sigma_{jet,p} \approx 50\text{mm}$ at $x/d = 50$.

5.3 Centerline velocity

The turbulent jet’s axis is positioned so that it intersects the x -axis of the FLDI thereby enabling the system to measure velocities in the x -direction. The jet is translated in the x (or streamwise) direction and data are collected at thirteen non-uniformly spaced locations from $x/d=1$ to $x/d=50$. Both FLDI signals are sampled for 13ms at 3MHz at each location. Each sample is divided into $10 \times 1.3\text{ms}$ segments and the velocity is computed for each segment as described in Sect. 3.3. The full experiment is repeated once so there are a total of 20 velocity measurements at each x/d location. Averaging these 20 measurements gives the centerline velocity at each x/d location, plotted in Fig. 24.

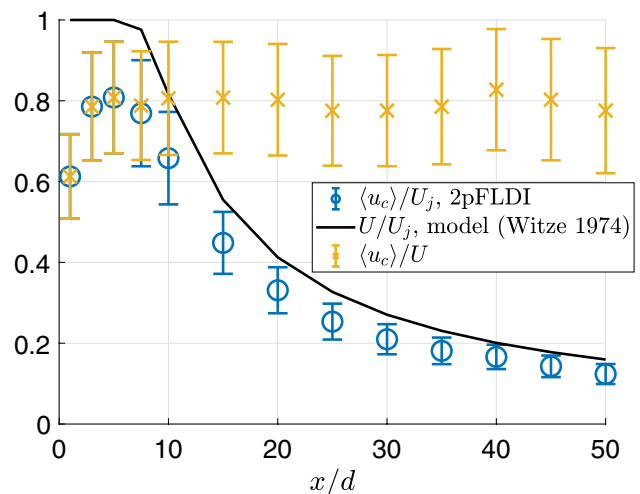


Fig. 24 2pFLDI convection velocity decay along jet centerline ($y/d = 0$, $z_0 = 0$; circles) compared to model of mean velocity decay by Witze (1974) (solid line) and 2pFLDI convection velocity to mean flow velocity ratio (crosses). Error-bars represent 95% confidence intervals

A brief divergence on the influence of the sampling window and filtering is useful before discussing the results. The average velocity determined using the method described in Sect. 3.3 is independent of segment length until the segment gets too small. For segment lengths below $0.7ms$ and at large x/d , the signal is not strong enough to produce a correlation peak above 0.1. Since structures may convect at different velocities in turbulent flows (Wills 1964), we also investigate frequency-dependant velocities found using the cross-spectrum technique described by Eq. 36-38. These velocities are plotted in Figs. 25 & 26. Before we discuss this, we are interested in how the mean 2pFLDI convection velocity compares to historical models and measurements of mean velocity.

Figure 24 compares centerline ($y = 0, z_0 = 0$) disturbance velocities (plotted with blue circles) to Witze’s jet velocity decay model (plotted with a solid line) (Witze 1974). Error bars represent 95% confidence intervals computed from the standard uncertainty of the 20 segments and the bias uncertainty of the beam pair separation using procedures outlined elsewhere (American Society of Mechanical Engineers 2006). The yellow data points in Fig. 24 (plotted using ‘x’) is the velocity measured using 2pFLDI divided by the predicted mean velocity from Witze. They show that velocities measured using 2pFLDI are 50–70% of Witze’s model at $x/d = 1$, and 70–90% of Witze’s model for $x/d \geq 3$. The behavior at $x/d = 1$ where measured convection velocities are $\sim 60\%$ of the jet exit velocity has been

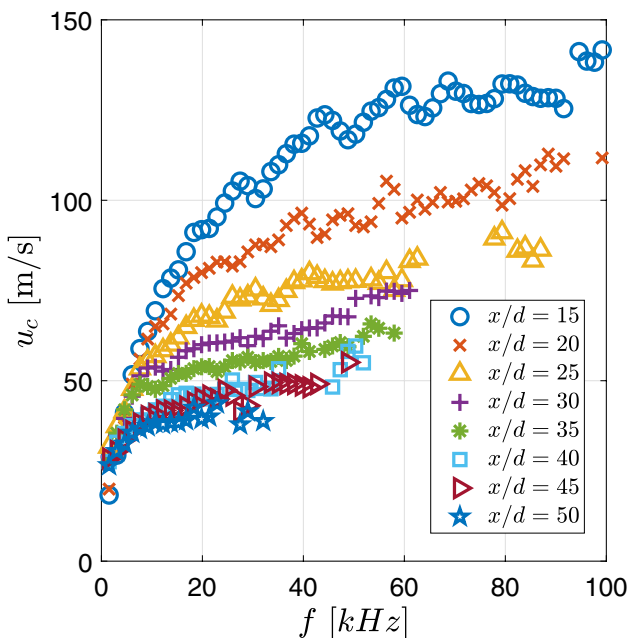


Fig. 25 Frequency-dependent convection velocities along the centerline ($y = 0, z_0 = 0$) of a round jet. Computed from the cross-spectra of 2pFLDI measurements (Eq. 36-38)

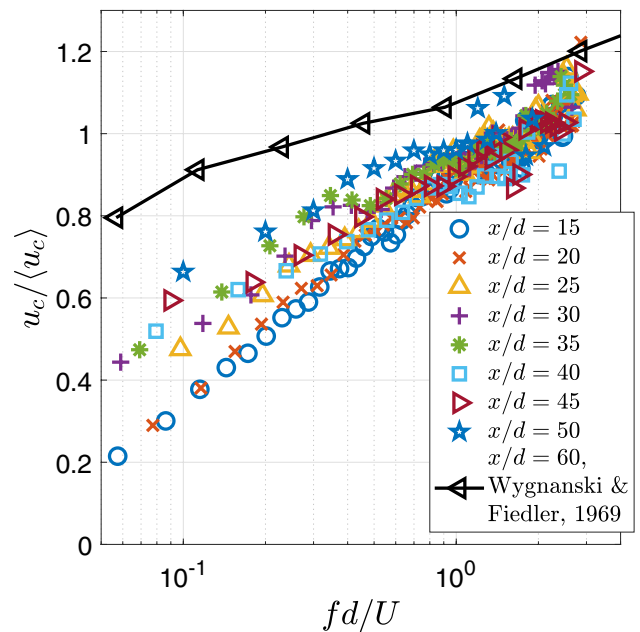


Fig. 26 Comparison of 2pFLDI and Wynanski & Fiedler’s hot wire scale-dependant convection velocities along the centerline ($y = 0, z_0 = 0$) of a round jet

observed by others (Fisher and Davies 1964; Kolpin 1964) and is likely due to disturbances in the circular mixing layer. Many have observed (Wills 1964; Wallace 2014; De Kat and Ganapathisubramani 2015) that the convection velocity found from the cross-correlation between fluctuating quantities measured by two probes depends on the probe separation distance. The reason is that convection velocity varies with scale. This biases the measurement towards scales which remain correlated across the distance and away from scales which dissipate across the distance. Therefore, a scale-dependant velocity is more meaningful.

Figure 25 shows frequency-dependent convection velocities computed from our FLDI measurements using Eq. 36-38. Measurements are made at the jet centerline using 13ms of data (collected at 3MHz) at each position downstream (x/d). The figure shows that velocity increases with frequency, decreases with x for $f > 5kHz$, and becomes independent of x as frequency goes to zero. This behavior is the result of two phenomena:

1. The scale dependence of FLDI’s sensitivity discussed in the previous section causes disturbances with low wavenumbers (corresponding to low frequency signals) to be more averaged across the span of the jet than disturbances with high wavenumber (high frequencies) causing the latter to be closer to the local centerline value.
2. low wavenumber disturbances convect slower than high wavenumbers along the jet centerline (Wills 1964; Wignanski and Fiedler 1969; Wallace 2014) because

the larger scales carry more momentum from the outer regions of the jet than the smaller scales.

To investigate this further, we compare our centerline velocity measurements (made at $y = 0, z_0 = 0$) to hot wire measurements in a round jet with similar Reynolds number ($Re \approx 10^5$) (Wygnanski and Fiedler 1969). The results are presented in Fig. 26. The vertical axis is velocity normalized by the average convection velocity over all scales found from the cross-correlation (Eq. 35) and the horizontal axis is a local Strouhal number: frequency normalized by jet diameter and local mean velocity found from Witze’s model. Wygnanski & Fiedler only report measurements at $x/d=2, 60$, and 90. They conclude that “all points collapse approximately on one curve” implying this trend is the same throughout the jet. We take their measurements at $x/d=60$ as the best comparison to ours ($x/d=15-50$) but do not observe collapse - especially at lower frequencies. This suggests that a comparison at equivalent downstream locations would be a good subject for future work. If we assume that Wygnanski & Fiedler’s measurements are indeed universal in the jet or that an FLDI measurements at $x/d=60$ would yield the same results as those at $x/d=50$, then one conclusion we can draw from Fig. 26 is the 2pFLDI measurements are biased low compared the hot-wire across nearly all frequencies and that the discrepancy is greater at low frequencies. This discrepancy clearly arises from differences in spatial / temporal sensitivity between FLDI and hot-wire anemometry. The length of the hot wire’s ‘sensitive region’ compared to the jet diameter is much smaller (1.2 mm in a 26 mm diameter jet) than that of the 2pFLDI (10-40 mm in a 3.2 mm diameter jet). Thus, slower moving structures away from the jet centerline will bias 2pFLDI measurements low compared to the hot-wire.

5.4 Velocity profiles

The variation of velocity transversely across the jet along the radial (y) direction is measured by collecting data at 27 non-uniformly spaced locations ranging from $y/d=-5$ to $y/d=5$. Once again, signals are sampled for 13ms at 3MHz. This time we compute the cross correlation (to get velocity) over the entire 13ms segment. These measurements are repeated at 8 downstream locations. The full experiment is repeated five times so that there are a total of 5 velocity measurements at each x/d and y/d and the average over all five tests is reported. The results are presented in Fig. 27. The results show how the jet broadens and the centerline jet velocity decreases as one moves downstream. Figure 28 shows velocity normalized by the centerline velocity ($U_{CL} = U(y = 0)$) as a function of normalized radial position (y/x). These results are compared to hot wire measurements by Wygnanski and Fiedler (1969) of convection velocity between two hot wires ($\langle U_{cb} \rangle$), plotted with dashed lines, as well as

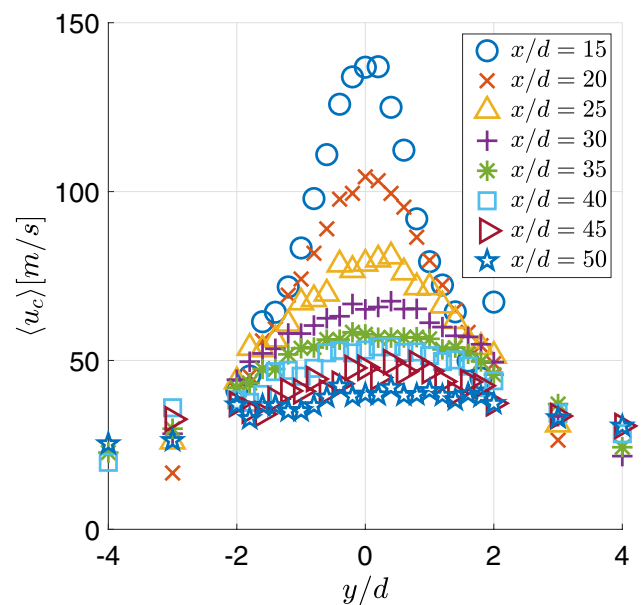


Fig. 27 Jet velocity profiles measured with 2pFLDI

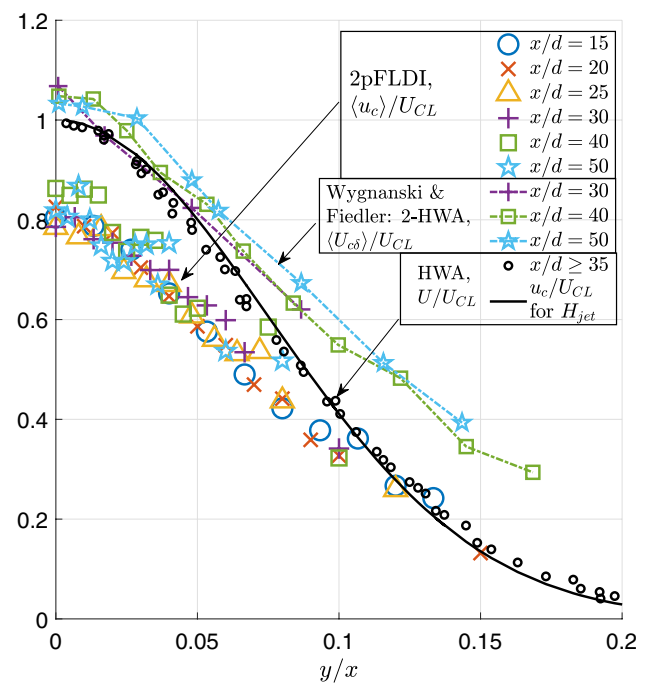


Fig. 28 Jet velocity profiles normalized by centerline value. Comparison to HWA measurements by Wygnanski and Fiedler (1969)

mean velocity measured by a single hot wire, plotted with small circles. Also plotted with a solid line is the Gaussian function (Eq. 31) used to evaluate the FLDI’s sensitivity to the jet, H_{jet} . Wygnanski & Fiedler’s measurements of $\langle U_{cb} \rangle$ are a good comparison to our mean 2pFLDI velocity, $\langle u_c \rangle$, because both measurements are found from the cross

correlation between two probes separated by a fixed distance. Figure 28 shows the 2pFLDI convection velocities follow a similar shape, but are consistently biased low by $\sim 20\%$ compared to the two-hot-wire convection velocities across all y/x . This is beyond the measurement uncertainty $\sim 10\%$ and is likely the result of large differences in spatial resolution between the two instruments, as discussed previously.

Next we note that the shape of the convection velocity ($\langle u_c \rangle$ and $\langle U_{c\delta} \rangle$) profile does not match that of the local mean velocity (U). On top of this, our model for u_c (a convection velocity given by Eq. 31, plotted in solid line in Fig. 28), follows the local velocity and not the measured convection velocity by 2pFLDI or two-hot-wire. This was found to produce the best collapse of recovered amplitude spectra, A_{jet} , when applied in the FLDI transfer function analysis. The reason for this discrepancy can be explained by Taylor's Hypothesis, which requires negligible mean shear to hold, i.e. when $k_x U \gg \frac{dU}{dy}$ (Lin 1953). Converting this to frequency, we have $f \gg \frac{1}{2\pi} \frac{dU}{dy}$. Evaluating for the mean velocity profile at $x/d = 25$, we find the maximum value of $\frac{1}{2\pi} \frac{dU}{dy}$ as $1.6kHz$ at $y = \sigma_{jet,u}$. At this location in the jet profile, only scales with $f \gg 1.6kHz$ are expected to convect with the local velocity, and throughout the rest of the jet this frequency cut-off will be lower. Comparing this to the time scales investigated in this work ($\sim 1 - 100kHz$) we see that most of the scales we are measuring satisfy this requirement. This explains why the mean velocity profile is a good model for convection velocities in this work. Furthermore, this suggests the spatial resolution of the measurement technique, and not the discrepancy between convection and mean velocity, has greater influence on the disagreement between 2pFLDI measurements and mean velocity profile presented in Fig. 28.

6 Conclusions and future work

A transfer function approach has been developed to interpret focused laser differential interferometer (FLDI) signals for the purpose of measuring density fluctuations in turbulent flows. A two point version of the technique capable of measuring velocities perpendicular to the interrogation beam has also been developed. Both techniques are applied to a canonical turbulent jet in an effort to better understand the FLDI instrument. The transfer functions and accompanying "sensitivity function" are capable of deconvolving the effects of beam separation and beam diameter from the true average disturbance amplitudes in the jet to within $\sim 50\%$ over $4 - 100kHz$. The critical advancement over previous work is accounting for velocity gradients in our model, i.e. $u_c(z)$. The findings

are important for several reasons. First, the transfer function approach is a lot simpler than the previous alternative which was to perform a full 3D ray tracing simulations of the experiment. Second, the transfer function approach makes it easier to understand the effects of changing design parameters like beam spacing on the performance of the instrument. Third, it enables one to quantify the FLDI's spatial resolution without the need to perform prior 'calibration' experiments where small disturbances are translated along the optical axis as in Parziale (2013) and Benitez et al. (2020). This simplifies the application of FLDI in future experiments.

The disagreement between 2pFLDI and hot wire velocity measurements in the jet appears to be due to depth of focus of the instrument which is relatively large - $\sim 10mm$ for the smallest scales and $\sim 40mm$ for the largest - compared to the jet width. Thus, low momentum fluid outside of the jet biases the velocity measurements low. Spatial resolution can be improved by increasing the convergence angle of the beams which, in turn, reduces the beam radius at the focus (w_0). Accurately measuring w_0 is critical for the analysis and a method for making this measurement using a beam profiler has been presented. Finally, we note that the 2pFLDI optical arrangement in this work was chosen to accommodate existing lab equipment. Future 2pFLDI set-ups should take more care to ensure parallel, or more nearly parallel, beam-pairs by keeping beam splitting prisms as close together as possible or by employing a set-up similar to that described by Bathel et al. (2020) or Neet et al. (2021).

One area for future work is to investigate the accuracy of transfer functions when the dispersion relation, $u_c(f)$, is used in place of velocity gradients, $u_c(z)$. This has the potential to eliminate one of the free parameters in the model because $u_c(f)$, unlike $u_c(z)$, is measured directly by 2pFLDI. Other areas of future work include verifying the transfer function approach in other jets, wind tunnels, and against FLDI simulations (Schmidt and Shepherd 2015; Lawson et al. 2020; Bathel et al. 2021), as well as modifying the beam radius transfer function to accommodate the non-circular beam profiles used in other work (Houpt and Leonov 2021; Weisberger et al. 2020). The larger goal is to validate the analytical model's ability to predict the influence of sidewall turbulent boundary/shear layers on the FLDI signal. The most challenging part will be modeling density disturbances and velocities in these boundary/shear layers.

A derivation of FLDI transfer functions, Eq. 18

Beginning with the argument of the z-axis integral in Eq. 17, which we will call Z, we have:

$$\begin{aligned}
 Z &= \int_0^{2\pi} \int_0^\infty I_0(r, \theta) \rho(\mathbf{x}_1, t) r dr d\theta \\
 &\quad - \int_0^{2\pi} \int_0^\infty I_0(r, \theta) \rho(\mathbf{x}_2, t) r dr d\theta
 \end{aligned} \tag{42}$$

Plug in the definition of beam intensity profile I_0 (Eq. 12), the density field model $\rho(x, y, z, t)$ (Eq. 10) and the definitions of the beam paths \mathbf{x}_1 and \mathbf{x}_2 (Eq. 15 and Eq. 16):

$$\begin{aligned}
 Z &= \int_0^{2\pi} \int_0^\infty \frac{2}{\pi w^2} \exp\left(-\frac{2r^2}{w^2}\right) g(z) \\
 &\quad \times \int_{-\infty}^\infty A(f) \exp\left[i\left(k_x\left(x + \frac{\Delta x_1}{2}\right) - 2\pi ft + \psi\right)\right] df r dr d\theta \\
 &\quad - \int_0^{2\pi} \int_0^\infty \frac{2}{\pi w^2} \exp\left(-\frac{2r^2}{w^2}\right) g(z) \\
 &\quad \times \int_{-\infty}^\infty A(f) \exp\left[i\left(k_x\left(x - \frac{\Delta x_1}{2}\right) - 2\pi ft + \psi\right)\right] df r dr d\theta
 \end{aligned} \tag{43}$$

Next, exchange the order of integration and re-arrange some terms:

$$\begin{aligned}
 Z &= g \int_{-\infty}^\infty A \int_0^\infty \frac{2r}{\pi w^2} \exp\left(-\frac{2r^2}{w^2}\right) \\
 &\quad \times \int_0^{2\pi} \exp\left[i\left(k_x\left(x + \frac{\Delta x_1}{2}\right) - 2\pi ft + \psi\right)\right] d\theta dr df \\
 &\quad - g \int_{-\infty}^\infty A \int_0^\infty \frac{2r}{\pi w^2} \exp\left(-\frac{2r^2}{w^2}\right) \\
 &\quad \times \int_0^{2\pi} \exp\left[i\left(k_x\left(x - \frac{\Delta x_1}{2}\right) - 2\pi ft + \psi\right)\right] d\theta dr df
 \end{aligned} \tag{44}$$

Re-arrange more terms and convert from Cartesian to polar coordinates using $x = r \cos(\theta)$:

$$\begin{aligned}
 Z &= g \int_{-\infty}^\infty A \left(\exp\left[i\left(k_x\left(x + \frac{\Delta x_1}{2}\right) - 2\pi ft + \psi\right)\right] \right. \\
 &\quad \times \int_0^\infty \frac{2r}{\pi w^2} \exp\left(-\frac{2r^2}{w^2}\right) \int_0^{2\pi} \exp(ik_x r \cos \theta) d\theta dr \\
 &\quad \left. - \exp\left[i\left(k_x\left(x - \frac{\Delta x_1}{2}\right) - 2\pi ft + \psi\right)\right] \right. \\
 &\quad \times \left. \int_0^\infty \frac{2r}{\pi w^2} \exp\left(-\frac{2r^2}{w^2}\right) \int_0^{2\pi} \exp(ik_x r \cos \theta) d\theta dr \right) df
 \end{aligned} \tag{45}$$

Re-arrange terms and evaluate the integral over θ :

$$\begin{aligned}
 Z &= g \int_{-\infty}^\infty A \exp\left[i(-2\pi ft + \psi)\right] \\
 &\quad \times \left(\exp\left[\frac{ik_x \Delta x_1}{2}\right] - \exp\left[\frac{-ik_x \Delta x_1}{2}\right] \right) \\
 &\quad \times \int_0^\infty \frac{2r}{\pi w^2} \exp\left(-\frac{2r^2}{w^2}\right) 2\pi J_0(k_x r) dr df
 \end{aligned} \tag{46}$$

where J_0 is the Bessel function of the first kind. Next, we evaluate the subtraction of the two exponential terms and evaluated the integral over beam radius, r . For more detail on this integral evaluation, see the next subsection, appendix 1.

$$\begin{aligned}
 Z &= g \int_{-\infty}^\infty A \exp\left[i(-2\pi ft + \psi)\right] \times \\
 &\quad 2i \sin\left(\frac{k_x \Delta x_1}{2}\right) \exp\left(-\frac{k_x^2 w^2}{8}\right) df.
 \end{aligned} \tag{47}$$

Finally, re-arrange to get the argument of the z-axis integral in Eq. 18.

A.1 Evaluation of integral over beam radius, r

Start with the integral over r in Eq. 46, which we will call \mathcal{R} :

$$\mathcal{R} = \int_0^\infty \frac{4r}{w^2} \exp\left(-\frac{2r^2}{w^2}\right) J_0(k_x r) dr \tag{48}$$

Using the definition of the Bessel function of the first kind, J_0 :

$$\mathcal{R} = \frac{4}{w^2} \int_0^\infty r \exp\left(-\frac{2r^2}{w^2}\right) \left[\sum_{n=0}^\infty \frac{(-k_x^2 r^2 / 4)^n}{(n!)^2} \right] dr \tag{49}$$

Expand out the sum:

$$\mathcal{R} = \frac{4}{w^2} \int_0^\infty r \exp\left(-\frac{2r^2}{w^2}\right) \left[1 - \frac{k_x^2 r^2}{4} + \frac{k_x^4 r^4}{64} - \dots \right] dr \tag{50}$$

Re-arrange:

$$\begin{aligned}
 \mathcal{R} &= \frac{4}{w^2} \left[\int_0^\infty r \exp\left(-\frac{2r^2}{w^2}\right) dr \right. \\
 &\quad \left. - \frac{k_x^2}{4} \int_0^\infty r^3 \exp\left(-\frac{2r^2}{w^2}\right) dr \right. \\
 &\quad \left. + \frac{k_x^4}{64} \int_0^\infty r^5 \exp\left(-\frac{2r^2}{w^2}\right) dr - \dots \right]
 \end{aligned} \tag{51}$$

Evaluate the integrals over r :

$$\mathcal{R} = \frac{4}{w^2} \left[\frac{w^2}{4} - \frac{k_x^2}{4} \left(\frac{w^4}{8}\right) + \frac{k_x^4}{64} \left(\frac{w^6}{8}\right) - \dots \right] \tag{52}$$

Finally, we have:

$$\mathcal{R} = 1 - \frac{k_x^2 w^2}{8} + \frac{k_x^4 w^4}{128} - \dots \tag{53}$$

Recognizing the Taylor's series expansion, we have

$$\mathcal{R} = \exp\left(-\frac{k_x^2 w^2}{8}\right). \tag{54}$$

Acknowledgements The authors would like to thank Mike Smith and AEDC Tunnel 9 staff for guidance and support. Additional thanks to the Air Force Office of Scientific Research support through the University of Maryland Hypersonic Center of Testing Excellence program, and the University of Maryland Clark Doctoral Fellowship Program.

References

- American Society of Mechanical Engineers (2006) Test Uncertainty. Tech. rep. ASME, New York, NY
- Anderson JD (2006) Hypersonic and High-Temperature Gas Dynamics, 2nd edn. American Institute of Aeronautics and Astronautics, Reston, VA
- Bathel BF, Weisberger JM, Herring GC, King RA, Jones SB, Kennedy RE, Laurence SJ (2020) Two-point, parallel-beam focused laser differential interferometry with a nomarski prism. *Appl Opt* 59(2):244. <https://doi.org/10.1364/ao.59.000244>
- Bathel BF, Weisberger JM, Herring GC, Jagannathan R, Johansen CT, Jones SB, Cavone AA (2021) Analysis of the Amplitude Response of a Two-Point and a Multi-Point Focused Laser Differential Interferometer. In: AIAA Scitech 2021 Forum, January, pp 1–17, <https://doi.org/10.2514/6.2021-0598>
- Benitez EK, Jewell JS, Schneider SP (2020) Focused laser differential interferometry for hypersonic flow instability measurements with contoured tunnel windows. *AIAA Journal* 1 PartF:1–22, <https://doi.org/10.2514/6.2020-1282>
- Birch B, Buttsworth D, Zander F (2020) Measurements of freestream density fluctuations in a hypersonic wind tunnel. *Exp Fluids* 61(7):1–13. <https://doi.org/10.1007/s00348-020-02992-w>
- Bonnet JP, Grésillon D, Taran JP (1998) Nonintrusive measurements for high-speed, supersonic, and hypersonic flows. *Annu Rev Fluid Mech* 30(1):231–273. <https://doi.org/10.1146/annurev.fluid.30.1.231>
- Born M, Wolf E (1980) Principles of Optics, 6th edn. Pergamon Press, New York
- Boutier A (1992) New Trends in Instrumentation for Hypersonic Research. 1, <https://doi.org/10.1007/s13398-014-0173-7.2>, arXiv: 1011.1669v3
- Buxton OR, de Kat R, Ganapathisubramani B (2013) The convection of large and intermediate scale fluctuations in a turbulent mixing layer. *Physics of Fluids* 25(12), <https://doi.org/10.1063/1.4837555>
- Ceruzzi AP, Callis BO, Weber DC (2020) Application of Focused Laser Differential Interferometry (FLDI) in a Supersonic Boundary Layer. In: AIAA Scitech Forum, pp 1–6
- De Kat R, Ganapathisubramani B (2015) Frequency-wavenumber mapping in turbulent shear flows. *J Fluid Mech* 783:166–190. <https://doi.org/10.1017/jfm.2015.558>
- Favre A, Gaviglio J, Dumas R (1967) Structure of velocity space-time correlations in a boundary layer. *Physics of Fluids* 10(S138), <https://doi.org/10.1063/1.1762432>
- Fisher MJ, Davies PO (1964) Correlation measurements in a non-frozen pattern of turbulence. *J Fluid Mech* 18(1):97–116. <https://doi.org/10.1017/S0022112064000076>
- Fulghum MR (2014) Turbulence Measurements in High-Speed Wind Tunnels using Focusing Laser Differential Interferometry. PhD thesis, The Pennsylvania State University
- Gillespie G, Ceruzzi A, Laurence S (2021) Multi-point Focused Laser Differential Interferometry for Noise Measurements in High-Speed Tunnels. In: AIAA Aviation 2021 Forum, <https://doi.org/10.2514/6.2021-2918>
- Gragston M, Price T, Davenport K, Zhang Z, Schmisser JD (2021) Linear array focused-laser differential interferometry for single-shot multi-point flow disturbance measurements. *Opt Lett* 46(1):154–157
- Gragston M, Price TJ, Davenport K, John D (2021b) An $m \times n$ FLDI Array for Single-Shot, Multipoint Disturbance Measurements in High-Speed Flows. AIAA Scitech 2021 Forum (January):1–16, <https://doi.org/10.2514/6.2021-0599>
- Hameed A, Parziale NJ (2021) Focused Laser Differential Interferometer Response to a Controlled Phase Object. In: AIAA Scitech 2021 Forum, January, pp 1–10, <https://doi.org/10.2514/6.2021-0602>
- Hinze JO, Van Der Hegge Zijnen BG (1949) Transfer of heat and matter in the turbulent mixing zone of an axially symmetrical jet. *Appl Sci Res* 1(1):435–461. <https://doi.org/10.1007/BF02120346>
- Haupt A, Leonov S (2021) Cylindrical Focused Laser Differential Interferometer. *AIAA Journal* pp 1–9, <https://doi.org/10.2514/1.J059750>
- Jewell JS, Hameed A, Parziale NJ, Gogineni SP (2019) Disturbance Speed Measurements in a Circular Jet via Double Focused Laser Differential Interferometry. AIAA Scitech 2019 Forum (January), <https://doi.org/10.2514/6.2019-2293>, <https://arc.aiaa.org/doi/10.2514/6.2019-2293>
- Kolpin MA (1964) The flow in the mixing region of a jet. *J Fluid Mech* 18(4):529–548. <https://doi.org/10.1017/S0022112064000398>
- Lawson JM (2021) Focused Laser Differential Interferometry. PhD thesis, California Institute of Technology
- Lawson JM, Neet MC, Grossman IJ, Austin JM (2020) Static and dynamic characterization of a focused laser differential interferometer. *Exp Fluids*. <https://doi.org/10.2514/6.2019-2296>
- Liepmann HW, Roshko A (1957) Elements of Gasdynamics, 1st edn. John Wiley & Sons Inc, New York
- Lin CC (1953) On Taylor's hypothesis and the acceleration terms in the Navier-Stokes equations. *Q Appl Math* 10(4):295–306. https://doi.org/10.1142/9789814415651_0011
- Neet MC, Lawson JM, Austin JM (2021) Design, alignment, and calibration of a focused laser differential interferometer. *Appl Opt* 60(26):7903. <https://doi.org/10.1364/ao.435112>
- Parziale N (2013) Slender-Body Hypervelocity Boundary-Layer Instability. PhD thesis, California Institute of Technology
- Parziale NJ, Shepherd JE, Hornung HG (2012) Reflected Shock Tunnel Noise Measurement by Focused Differential Interferometry. 42nd AIAA Aerospace Sciences Meeting (June):1–10
- Parziale NJ, Shepherd JE, Hornung HG (2013) Differential interferometric measurement of instability in a hypervelocity boundary layer. *AIAA J*. <https://doi.org/10.2514/1.J052013>
- Parziale NJ, Shepherd JE, Hornung HG (2014) Free-stream density perturbations in a reflected-shock tunnel. *Experiments in Fluids* 55(2), <https://doi.org/10.1007/s00348-014-1665-0>
- Pate SR, Schueler CJ (1969) Radiated aerodynamic noise effects on boundary-layer transition in supersonic and hypersonic wind tunnels. *AIAA J* 7(3):450–457
- Poon TC, Kim T (2006) Engineering Optics with MATLAB. World Scientific Publishing Co., Singapore
- Reshotko E (2008) Transition issues for atmospheric entry. *J Spacecr Rocket* doi 10(2514/1):29777
- Sanderson SR (2005) Simple, adjustable beam splitting element for differential interferometers based on photoelastic birefringence of a prismatic bar. *Rev Sci Instrum* 76(11):113703. <https://doi.org/10.1063/1.2132271>
- Schmidt BE, Shepherd JE (2015) Analysis of focused laser differential interferometry. *Appl Opt*. <https://doi.org/10.1364/AO.54.008459>
- Schneider SP (2001) Effects of high-speed tunnel noise on laminar-turbulent transition. *J Spacecr Rocket* 38(3):323–333. <https://doi.org/10.2514/2.3705>
- Settles GS, Fulghum MR (2016) The focusing laser differential interferometer, an instrument for localized turbulence measurements in refractive flows. *J Fluid Eng* doi 10(1115/1):4033960
- Shea JF (1988) Report of the Defense Science Board Task Force on the NATIONAL AEROSPACE PLANE (NASP). Tech. rep, Defense Science Board

- Siegman AE (1986) Lasers. University Science Books, Sausalito
- Smeets G (1977) Flow Diagnostics by Laser Interferometry. IEEE Transactions on Aerospace and Electronic Systems (2)
- Smeets G, George A (1971) Gas-dynamic investigations in a shock tube using a highly sensitive interferometer. IEEE Transactions on Aerospace and Electronic Systems 298(0704)
- Smeets G, George A (1973) Laser-differential interferometer applications in gas dynamics. IEEE Transactions on Aerospace and Electronic Systems 298(0704)
- Taylor GI (1938) The spectrum of turbulence. Proceedings of the Royal Society 164(919)
- Wallace JM (2014) Space-time correlations in turbulent flow: a review. Theor Appl Mech Lett 4(2):022003. <https://doi.org/10.1063/2.1402203>
- Weisberger JM, Bathel BF, Herring GC, Buck GM, Jones SB, Cavone AA (2020) Multi-point line focused laser differential interferometer for high-speed flow fluctuation measurements. Appl Opt 59(35):11180–11195
- Weisberger JM, Bathel BF, Herring GC, Buck GM (2021) Two-line focused laser differential interferometry of a flat plate boundary layer at mach 6. In: AIAA Scitech 2021 Forum, January, pp 1–29, <https://doi.org/10.2514/6.2021-0601>
- Welch PD (1967) The use of fast fourier transform for the estimation of power spectra: a method based on time aver. aging Over Short, Modified Periodograms $I_k(f_n) = -I A h (\%) [a k. Tech. Rep. 2$
- Wills JA (1964) On convection velocities in turbulent shear flows. J Fluid Mech 20(3):417–432. <https://doi.org/10.1017/S002211206400132X>
- Witze PO (1974) Centerline velocity decay of compressible free jets. AIAA J 12(4):417–418. <https://doi.org/10.2514/3.49262>
- Wynanski I, Fiedler H (1969) Some measurements in the self-preserving jet. J Fluid Mech 38(03):577. <https://doi.org/10.1017/S0022112069000358>

Publisher's Note Springer Nature remains neutral with regard to jurisdictional claims in published maps and institutional affiliations.